Australian Government
Department of Defence
Defence Science and
Technology Organisation

Approximate Invariance of the Inverse of the Covariance Matrix and the Resultant Pre-built STAP Processor

Yunhan Dong

Electronic Warfare and Radar Division
Systems Sciences Laboratory

DSTO-RR-0291

ABSTRACT

Space-time adaptive processing (STAP) has been proven to be optimum in scenarios where an airborne phased-array radar is used to search for moving targets. The STAP requires the inverse of the covariance matrix (ICM) of undesired signals. The computation of the real-time ICM is impractical at current computer speeds. Proposing two Theorems, this report indicates that the ICM is approximately invariant if radar and platform parameters remain unchanged. A pre-built STAP (PSTAP) processor is then proposed. Both the simulated data from a generic airborne phased array radar model and real data collected by the multi-channel airborne radar measurement (MCARM) system are processed to verify the processor. Results indicate that the performance of the proposed PSTAP processor is the same as that of the real-time STAP processor.

Published by

DSTO Systems Sciences Laboratory
PO Box 1500
Edinburgh South Australia 5111 Australia

Telephone: (08) 8259 5555
Fax: (08) 8259 6567

AR-013-364
March 2005

APPROVED FOR PUBLIC RELEASE

Approximate Invariance of the Inverse of the Covariance Matrix and the Resultant Pre-built STAP Processor (U)

Executive Summary

The central task for an airborne early warning & control (AEW&C) radar is to detect moving targets in the presence of undesired signals such as surface clutter and directional broadband noise jamming. Within certain conditions space-time adaptive processing (STAP) has been proven to be optimum in scenarios where an airborne phased-array radar is used to search for moving targets. If the covariance matrix (CM) of undesired signals including clutter, jamming and thermal noise can be determined (measured or estimated), the upper limit of the coherent processing gain for desired target signals can be achieved using STAP while the undesired signals are sufficiently suppressed. However, computation of the inverse of the covariance matrix (ICM) becomes a bottleneck which prevents the fully adaptive STAP from real-time implementation at current computer speeds. Hence many operational systems must use alternative less computationally intensive processes, such as the one proposed in this report.

Proposing two Theorems, this report indicates that the ICM is approximately invariant when radar and platform parameters remain unchanged. Based on this, the following conclusions are deduced:

- For clutter, STAP needs to adapt only to system parameters (both radar and platform). Variations in clutter intensity, which may incur significant variations in the elements of the CM, cause little variations in the elements of the ICM;
- For jamming, STAP needs to adapt only to the bearing of jamming. Variations in jamming intensity, which may incur significant variations the in elements of the CM, causes little variations in the elements of the ICM.

Because the construction of optimum weighting vectors only requires knowledge of the ICM, the approximate invariance of the ICM naturally results in a proposal for constructing a pre-built space-time non-adaptive processing (PSTAP) processor. PSTAP is not adaptive processing in the broad meaning, as no adaptive processor can be built a priori. However, because it does not require knowledge of the clutter environment, the PSTAP processor can be pre-built, and still perform the same as the STAP processor as long as the system (radar and platform) parameters are known.

Prior to the mission, libraries of the jamming filters as well as optimum weighting vectors may be constructed either purely from modelling or based on test flight measurements. Each weighting vector is optimal to a particular operational situation. During the mission, first the collected data are analysed to determine the presence of jamming by other means. Appropriate jamming filters are called from the library or

beamforming techniques are used to suppress the jamming. The jamming-free data are then simply multiplied with the appropriate optimum weighting vectors from the library to generate the result.

If a real radar system is difficult to model (for instance, the array may not be rigorously linear and the effect of the platform on the antenna system may be difficult to model etc), the library may be pre-built based on data collected from previous missions. Because of the nature of its approximate invariance, the ICM from different clutter environments should be approximately the same for the same set of radar and platform parameters. Therefore, the optimum weighting vectors obtained from previous missions can be directly used for future missions, irrespective of clutter environments, provided that the radar and platform parameters remain unchanged.

There are usually a large number of possible combinations of radar and platform parameters, so a large number of pre-built optimum weighting vectors will be required. If the radar pulse repetition frequency (PRF) is linked to the platform velocity to maintain the number of clutter foldovers to be constant, the number of combinations can be significantly reduced. Also because the ICM is not sensitive to changes in steering angle which varies from range bin to range bin, the same set of optimum weighting vectors can be applied to many range bins with little signal to interference and noise ratio (SINR) loss.

A robust analysis for PSTAP has been carried out. Uncertainties incurred in steering angles possibly caused by an undulating terrain surface have been studied. It has been shown that the PSTAP SINR loss compared to STAP SINR is normally only about 0.2-0.5dB even for a highly undulating terrain.

Numerical examples are presented. The first numerical example is for a generic airborne radar model. Cases of clutter coefficients randomly fluctuating up to $\pm 15dB$ (simulating extreme inhomogeneous environments) are compared to the usual case of the constant clutter coefficient (simulating an ideally homogenous clutter environment) showing that the resultant ICMs are almost identical. The correlation coefficient r^2 for all pairs of ICMs compared are higher than 0.99. The performance of the PSTAP processor is compared to the real-time STAP processor, and results are the same for all scenarios.

The report then examines the PSTAP processor applied to real data collected by the multi-channel airborne radar measurements (MCARM) system. Temporal and spatial correlation is considered in order to build a realistic and appropriate PSTAP processor. It is shown that decorrelation in the MCARM data is primarily caused by range ambiguity and clutter intrinsic motion. Finally the PSTAP processor is compared to the conventional STAP processor for detecting embedded small target signals. It is shown that the performance of PSTAP is the same as that of STAP for the cases studied. A moving target has been first detected in the MCARM data set by the application of the PSTAP process.

The PSTAP is also applied to process airborne data generated by the high fidelity airborne radar simulation software, Rome Laboratory Space-Time Adaptive Processing (RLSTAP), details will be reported in the future.

Author

Yunhan Dong
Electronic Warfare and Radar Division

Dr Yunhan Dong received his Bachelor and Master degrees in 1980s in China and his PhD in 1995 at UNSW, Australia, all in electrical engineering. He then worked at UNSW from 1995 to 2000, and Optus Telecommunications Inc from 2000 to 2002. He joined DSTO as a Senior Research Scientist in 2002. His research interests are primarily in radar signal and image processing, and radar backscatter modelling. Dr Dong was a recipient of both Postdoctal Research Fellowships and Research Fellowships from the Australian Research Council.

Contents

1. INTRODUCTION 1

2. FORMULATION OF THE COVARIANCE MATRIX OF UNDESIRED SIGNALS2
2.1 Clutter 3
2.2 Jamming 7
2.3 Thermal Noise 8
2.4 Covariance Matrix of Undesired signals 8

3. SPACE-TIME ADAPTIVE PROCESSING 9
3.1 Fully Adaptive STAP 9
3.2 Partially Adaptive STAP 11

4. APPROXIMATE INVARIANCE OF THE INVERSE OF THE COVARIANCE MATRIX 16
4.1 Theorem 1 16
4.1.1 Example 1 18
4.1.2 Example 2 20
4.1.3 Examples 3, 4 and 5 22
4.2 Theorem 2 25
4.2.1 Examples 27
4.3 Robust Analysis 28
4.4 Significance 34
4.5 Interpretation 34
4.6 Implementation 35
4.6.1 Prior to the mission 35
4.6.2 During the mission 36

5. NUMERICAL RESULTS 36
5.1 Results from a Generic Model 36
5.2 Results from MCARM Data 39
5.2.1 Forming the Covariance Matrix Using the SMI Method 40
5.2.2 Crab Angle Correction 42
5.2.3 Temporal and Spatial Decorrelation Effects 43
5.2.4 Results 48

6. CONCLUSIONS 56

7. ACKNOWLEDGEMENT 58

8. REFERENCES 59

APPENDIX A: MCARM SYSTEM 61

1. Introduction

The central task for an airborne early warning & control (AEW&C) radar is to detect moving targets in the presence of undesired signals such as clutter (echoes from the Earth surface) and directional broadband noise jamming. Subject to certain conditions, space-time adaptive processing (STAP) has been proven to be optimal in such scenarios where an airborne pulsed Doppler phased array radar is used in searching for moving targets. If the covariance matrix (CM) of the undesired signals including clutter, jamming and thermal noise can be determined (measured or estimated), the upper limit of the coherent processing gain for the desired target signal can be achieved using STAP while the undesired signals are sufficiently suppressed (Ward, 1994, Klemm, 2002, Wirth, 2001). However, in real-time implementation of STAP, the computation of the inverse of the covariance matrix (ICM) becomes a bottleneck which makes the fully adaptive STAP infeasible at current computer speeds. Numerous algorithms, aimed at reducing the dimensionality of the CM in both the spatial and temporal domains, have then been proposed to minimise the computation time to satisfy the real-time requirement while maintaining the coherent processing at or close to the optimum level.

This report presents a significant finding, the approximate invariance of the ICM. Based on this, use of a pre-built STAP (PSTAP) processor for real-time processing is proposed. The PSTAP is not an adaptive processor in the broad meaning of adaptive processing where the processor automatically adapts to any changes in both the system (radar and platform) parameters and the environment (clutter). However, it can cope with changes in clutter provided that the radar and platform parameters remain unchanged. For convenience, the name of PSTAP is used. The prefixal 'pre-built' indicates that the processor is not adaptive in a broad sense as no adaptive processor can be pre-built, while the suffixal 'STAP' implies that the processor is constructed in a STAP fashion. The idea of PSTAP is to construct a set of weighing vectors a priori, either by theoretical modelling or using flight data. Each weighting vector is equivalent to a fully STAP weighting vector for a specific situation. Using such a processor the computational bottleneck is eventually removed thoroughly. Theoretically, if the system (radar and platform) parameters are known, the proposed PSTAP can achieve the same coherent processing gain as real-time STAP (the knowledge of clutter is not required). In reality, due to the fact that the CM for the real-time STAP is difficult to obtain accurately, the PSTAP may even achieve better results if all system parameters required for the construction of the processor are known precisely.

Various tapering (window) functions can be applied to both the spatial and temporal domains in the STAP. The pros and cons of window functions are well known. This report does not include the application of window functions, as their effects can be readily anticipated.

Section 2 starts formulating the CM of undesired signals for a generic airborne phased-array antenna in the side-looking situation. Section 3 briefly summarises the fully and partially adaptive STAP algorithms. A unique characteristic, the invariance of the ICM, is presented in Section 4. Two Theorems are given which in turn form a base for the

construction of the PSTAP processor. A robust analysis for the PSTAP processor is also presented in Section 4 to deal with uncertainties. Numerical examples of applying the PSTAP processor to a generic model (the same model used by Ward, 1994) and to the data collected by a real airborne system, the multi-channel airborne radar measurement (MCARM) system, are presented in Section 5 in supporting verification of the PSTAP processor. Section 6 concludes the report.

2. Formulation of the Covariance Matrix of Undesired Signals

The undesired signals in the radar environment under consideration include clutter (echoes from the Earth surface), directional broadband noise jamming, and thermal noise. Their modelling has been well documented (Ward, 1994, Klemm, 2002) and is briefly summarised in this Section.

Mathematical notations follow the convention (Ward, 1994). Italic typeface symbols stand for scalars; lowercase and uppercase boldface symbols for vectors and matrices, respectively. Subscripts T, * and H denote the operations of transpose, complex conjugate and Hermitian transpose, respectively. The symbol $\otimes$ refers to the Kronecker matrix product. Finally the symbol $E\{\cdot\}$ denotes the expected value of a random quantity.

An airborne linear phased array antenna looking at the broadside is the default configuration. In particular, let a platform be moving in the x-direction at a speed of v_a, a linear antenna array with N elements be parallel with the direction of motion and look at the broadside y-direction, as shown in Figure 1. Symbols H, R, θ and ϕ denote platform height, range, elevation angle and azimuth angle, respectively.

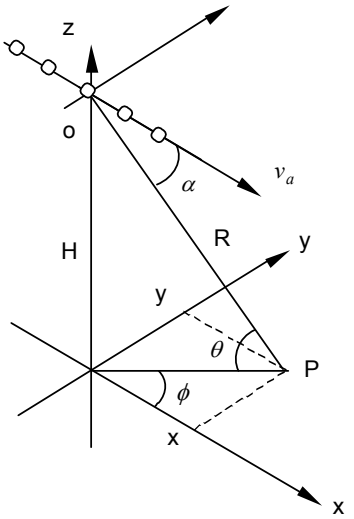

Figure 1: Geometry of a linear airborne antenna array.

Because the receive antenna consists of N elements, the received signal, after being down processed to the baseband, for a given range bin, also consists of N complex components (I and Q values) for every transmitted pulse. Assuming that there are M pulses in a coherent processing interval (CPI), the received signal, which is comprised of MN complex components in total, is usually expressed by a $MN \times 1$ vector (often referred to as a space-time snapshot) as,

$$\boldsymbol{\chi} = \begin{bmatrix} \chi_{0,0} & \cdots & \chi_{0,N-1} & \cdots & \chi_{M-1,0} & \cdots & \chi_{M-1,N-1} \end{bmatrix}^T \tag{1}$$

where χ_{mn} is the received signal at the n^{th} antennal element ($n = 0, \cdots, N-1$) for the m^{th} pulse ($m = 0, \cdots, M-1$). Without loss of generality, a snapshot, $\boldsymbol{\chi}$, may contain the desired signal component, $\boldsymbol{\chi}_t$, as well as the undesired signal components of clutter, $\boldsymbol{\chi}_c$, jamming, $\boldsymbol{\chi}_j$, and noise, $\boldsymbol{\chi}_n$.

2.1 Clutter

We assume at this stage of the analysis that the pulse repetition frequency (PRF) is sufficiently low that range is sampled unambiguously. We further neglect the effects of the intrinsic motion of clutter. These assumptions lead to the first-order general clutter model (Ward, 1994). Spatial and temporal correlations due to range ambiguity (range fold-over), the intrinsic motion of clutter and the motion of platform will be dealt with later in Section 5 where live airborne radar data are processed. The space-time snapshot of clutter for the first-order general clutter model can be written as a summation (integral) of clutter echoes from a constant range ring as (Ward, 1994),

$$\boldsymbol{\chi}_c = \sum_{k=1}^{N_c} \alpha_k \mathbf{v}(\vartheta_k, \varpi_k) \tag{2}$$

where α_k is a random clutter echo from the k^{th} clutter patch at the steering angle ϑ_k, and $\mathbf{v}(\vartheta_k, \varpi_k)$ the corresponding space-time steering vector.

$$\mathbf{v}(\vartheta_k, \varpi_k) = \mathbf{b}(\varpi_k) \otimes \mathbf{a}(\vartheta_k) \tag{3}$$

where $\mathbf{a}(\vartheta_k)$ and $\mathbf{b}(\varpi_k)$ are spatial and temporal steering vectors, respectively, as

$$\mathbf{a}(\vartheta_k) = \begin{bmatrix} 1 & \exp(-j2\pi\vartheta_k) & \cdots & \exp(-j2\pi(N-1)\vartheta_k) \end{bmatrix}^T \tag{4}$$

$$\mathbf{b}(\varpi_k) = \begin{bmatrix} 1 & \exp(-j2\pi\beta\vartheta_k) & \cdots & \exp(-j2\pi\beta(M-1)\vartheta_k) \end{bmatrix}^T \tag{5}$$

$$\vartheta_k = \frac{d}{\lambda}\cos\theta\cos\phi_k \tag{6}$$

where d is the antenna element space, λ the radar frequency, θ and ϕ_k are the elevation angle and the azimuth angle, respectively, for the kth clutter patch. $\beta = 2v_a T_r / d$ is the ratio of the normalised Doppler frequency to the normalised spatial frequency. $\beta = 1$ means that the platform moves one element space d, in one pulse repetition interval (PRI). Sometimes β is also referred to as the number of clutter fold-overs.

The clutter amplitude satisfies $E\{|\alpha_k|^2\} = \sigma^2\xi_k$, where σ^2 is the system thermal noise, and ξ_k is the single-pulse clutter-to-noise ratio (CNR) for a single antenna element on receive, whose value may be determined from the radar equation as,

$$\xi_k = \frac{P_t T_p G(\theta,\phi_k) g(\theta,\phi_k) \lambda^2 \sigma_0(\theta,\phi_k) A_k}{(4\pi)^3 L_s R^4} \tag{7}$$

where P_t is the transmit power, T_p the pulse width. G and g are the full array transmit power gain and the element receive power gain, respectively. A_k is the clutter patch area and σ_0 the backscattering coefficient for the area. L_s denotes the total loss in the radar system.

With a further assumption that clutter echoes are uncorrelated from patch to patch, the clutter CM is therefore,

$$\mathbf{R}_c = E\{\boldsymbol{\chi}_c \boldsymbol{\chi}_c^H\} = \sigma^2 \sum_{k=1}^{N_c} \xi_k \mathbf{V}_k \mathbf{V}_k^H = \mathbf{V}\boldsymbol{\Sigma}_c \mathbf{V}^H \tag{8}$$

where $\mathbf{V} = (\mathbf{v}_1 \quad \cdots \quad \mathbf{v}_{N_c})$ and $\boldsymbol{\Sigma}_c = \sigma^2 diag(\xi_1 \quad \cdots \quad \xi_{Nc})$.

Since antenna gain patterns in (7) are system dependent, we need to further define system parameters in order to compute the clutter CM. Parameters for the generic radar system model used in this report are the same as those used by Ward (1994), and are given below.

- Equal-spaced linear planner antenna array with half wavelength element spacing ($w = d/\lambda = 0.5$);
- Number of elements in azimuth: 18;
- Number of elements in elevation: 4;
- Element pattern: cosine with a –60dB backlobe level;
- Transmitter tapering: uniform;
- Platform height 9000 m;
- Range 130 km;
- PRF: 300 Hz;
- Number of clutter fold-over $\beta = 1$;

- Number of pulses in a CPI $M = 18$.

Based on these parameters, it is straightforward to obtain the transmit antenna pattern $G(\theta,\phi_k)$, and the receive element pattern $g(\theta,\phi_k)$ (Wirth, 2001).

With the assumption of the clutter coefficient σ_0 to be constant, $G(\theta,\phi_k)$ and $g(\theta,\phi_k)$ for a patch positioned at (θ,ϕ_k) can be determined from the geometry relationship between the illuminated patch and the antenna orientation (Note that the antenna's elevation angle and azimuth angle are generally not coincident with the elevation angle and azimuth angle of the illuminated patch, but can be numerically or analytically determined for the given geometry). Figure 2 shows the normalised clutter pattern $\mathbf{\Sigma}_c$ for a ring of R = *130 km*, assuming the clutter coefficient $\sigma_0(\theta,\phi_k)$ to be constant and the antenna looking horizontally. It can be seen that the backlobe is 120dB down (two-way) compared to the frontlobe, because we assume the backlobe of the antenna element pattern is 60dB down (one-way) from the frontlobe. In reality, the measured backlobe level will be limited by the receiver's thermal noise level, and will never be as low as those shown in Figure 2. However, because the thermal noise is included in the modelling, there is no need to further modify these theoretical backlobe values. Levels of backlobe, if below the thermal noise level, will eventually be masked.

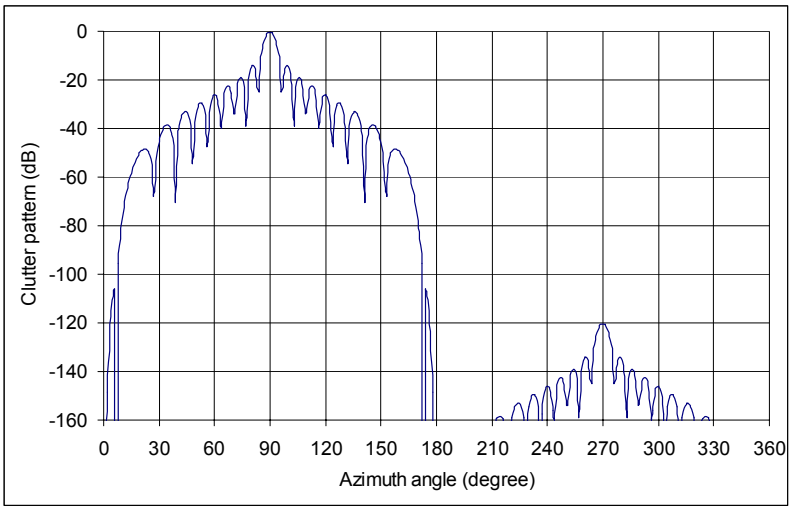

Figure 2: Clutter pattern received from a ring of R = 130 km, assuming the clutter coefficient $\sigma_0(\theta,\phi_k)$, $k = 1,\cdots,N_c$, *to be constant.*

The structure of $\mathbf{R}_c$ given by (8) has a so-called Toeplitz-block-Toeplitz pattern (Ward 1994). It is also a Hermitian and usually low rank matrix. The rank of $\mathbf{R}_c$ is given by Brennan's Rule as (Brennan and Staudaher, 1992, Ward, 1994),

$$N_r = \text{int}\{N + \beta(M-1)\} \tag{9}$$

Figure 3 shows the Toeplitz-block-Toeplitz pattern of the clutter CM. Only the magnitude (normalised to 1) is shown in the figure. Shown in Figure 4 is the rank of $\mathbf{R}_c$ which varies as a function of β.

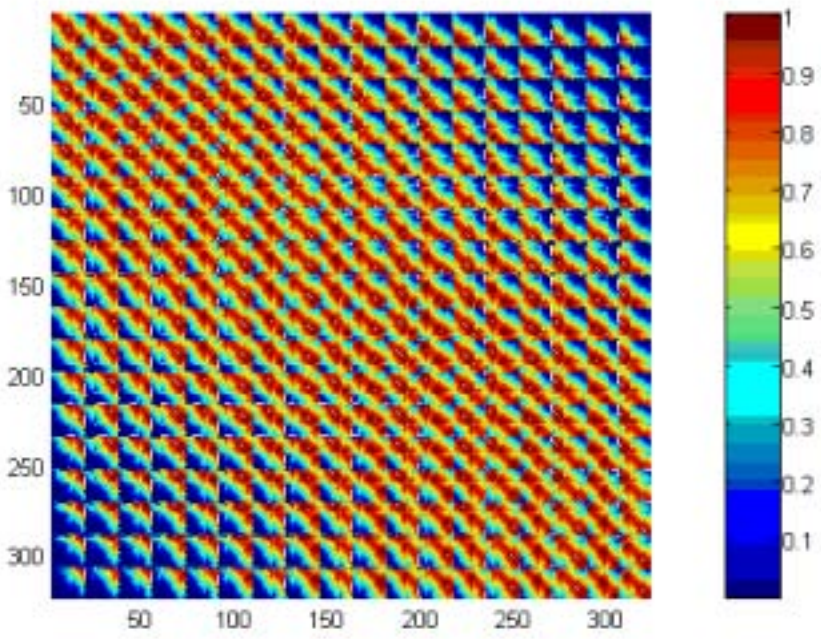

Figure 3: Clutter covariance matrix has a Teoplitz-block-Toeplitz pattern.

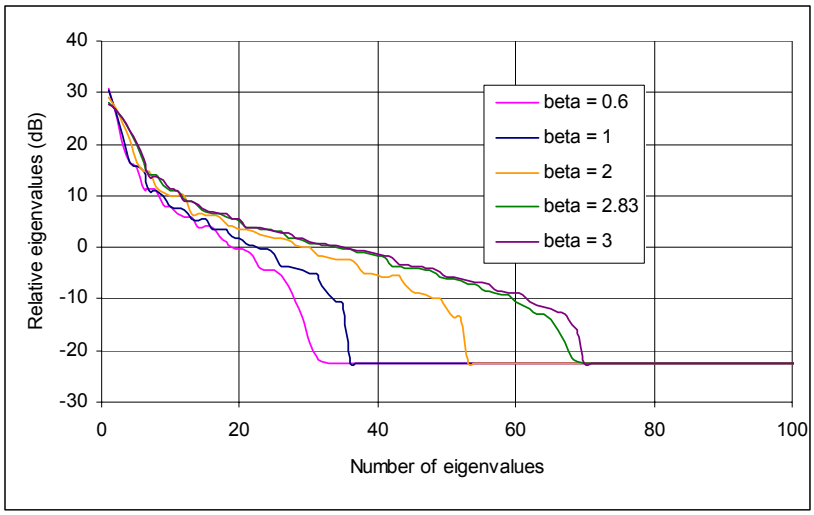

Figure 4: The number of eigenvalues of the clutter covariance matrix varies with the number of clutter fold-overs (side-looking array, $N = M = 18$). Only the first 100 of 324 eigenvalues are shown.

2.2 Jamming

Only directional broadband noise jamming is considered. The jamming signal is assumed to be a point target spatially, correlated from element to element spatially but uncorrelated from pulse to pulse temporally. The space-time snapshot of the jamming signal can be written as,

$$\chi_j = \boldsymbol{\alpha}_j \otimes \mathbf{a}_j \tag{10}$$

where $\mathbf{a}_j$ is the spatial steering vector corresponding to the jammer's location, and $\boldsymbol{\alpha}_j = [\alpha_0 \quad \alpha_1 \quad \cdots \quad \alpha_{M-1}]^T$ is a $M \times 1$ vector containing random jamming signals measured by the pulse train in a CPI, and satisfies

$$E\{\alpha_{m1}\alpha_{m2}^*\} = \sigma^2 \xi_j \delta_{m1-m2} \tag{11}$$

where ξ_j is the jammer-to-noise ratio (JNR). The jamming CM is therefore,

$$\mathbf{R}_j = E\left\{\boldsymbol{\chi}_j \boldsymbol{\chi}_j^H\right\} = \sigma^2 \xi_j \mathbf{I}_M \otimes \left(\mathbf{a}_j \mathbf{a}_j^H\right) \tag{12}$$

where I_M is an $M \times M$ identity matrix.

Multiple jamming signals are normally uncorrelated, so the CM of multiple jamming signals is the sum of the CM of each jamming signal as,

$$\mathbf{R}_j = E\left\{\boldsymbol{\chi}_j \boldsymbol{\chi}_j^H\right\} = \sigma^2 \sum_j \xi_j \mathbf{I}_M \otimes \left(\mathbf{a}_j \mathbf{a}_j^H\right) \tag{13}$$

Figure 5 shows the normalised jamming CM for the case of two jamming signals of equal intensity, located at $\left(0^0, 65^0\right)$ and $\left(0^0, 130^0\right)$, respectively.

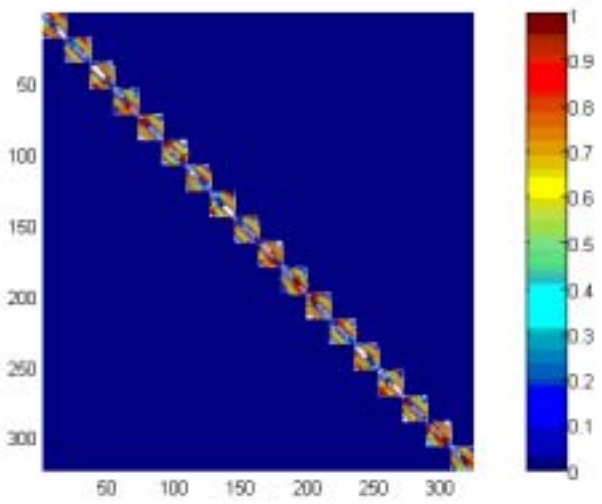

Figure 5: The covariance matrix of two independent jamming signals, each of which is assumed to be spatially correlated and temporally uncorrelated.

2.3 Thermal Noise

The dominant thermal noise is the receiver noise (usually limited by the thermal noise of the first amplifier). If each element has its own receiver, then the noise process in each element is mutually uncorrelated. The snapshot of noise can be written as,

$$\boldsymbol{\chi}_n = [\,\alpha_{0,0} \quad \cdots \quad \alpha_{0,N-1} \quad \cdots \quad \alpha_{M-1,0} \quad \cdots \quad \alpha_{M-1,N-1}\,]^T \tag{14}$$

Its temporally and spatially uncorrelated nature satisfies,

$$E\{\alpha_{m1,n1}\alpha^*_{m2,n2}\} = \sigma^2\delta_{m1-m2}\delta_{n1-n2} \tag{15}$$

The CM is therefore,

$$\mathbf{R}_n = E\left\{\boldsymbol{\chi}_n\boldsymbol{\chi}_n^H\right\} = \sigma^2\mathbf{I}_{MN} \tag{16}$$

2.4 Covariance Matrix of Undesired signals

Clutter, jamming and thermal noise are mutually uncorrelated, so the CM contributed together by clutter, jamming and thermal noise is,

$$\mathbf{R}_u = \mathbf{R}_c + \mathbf{R}_j + \mathbf{R}_n \tag{17}$$

From now on, unless specified, the covariance matrix given by Equation (17) is simply referred to as the CM, and its inversion, the ICM.

3. Space-Time Adaptive Processing

3.1 Fully Adaptive STAP

Suppose that the data snapshot at range of interest contains a target signal as,

$$\boldsymbol{\chi} = \boldsymbol{\chi}_t + \boldsymbol{\chi}_c + \boldsymbol{\chi}_j + \boldsymbol{\chi}_n \tag{18}$$

where

$$\boldsymbol{\chi}_t = \alpha_t \mathbf{v}_t \tag{19}$$

α_t and $\mathbf{v}_t$ are the amplitude and steering vector, respectively, of the target signal.

It is well known that the optimum space-time weighting vector for detecting the desired target signal with a steering vector of $\mathbf{v}_t$ is (Compton, Jr., 1988),

$$\mathbf{w}_{opt} = \gamma \mathbf{R}_u^{-1} \mathbf{v}_t \tag{20}$$

where γ is an arbitrary scalar. The output of the STAP processor is the product of the Hermitian transpose of the weighting vector times the data snapshot,

$$y = \mathbf{w}_{opt}^H \boldsymbol{\chi} \tag{21}$$

The coherent processing gain of the optimum processor approaches the upper limit, $10\log_{10}(MN)$ dB, for deterministic signals whose bearings differ from the jamming bearings, and whose Doppler frequencies differ from the clutter Doppler frequency at the looking direction.

The signal to interference and noise ratio (SINR) is defined as the output target power to the output interference and noise power,

$$SINR = \frac{|y_t|^2}{|y_u|^2} = \frac{\sigma^2 \xi_t \left| \mathbf{w}_{opt}^H \mathbf{v}_t \right|^2}{\mathbf{w}_{opt}^H \mathbf{R}_u \mathbf{w}_{opt}} \tag{22}$$

where $E\{|\alpha_t|^2\} = \sigma^2 \xi_t$.

The performance of the processor sometimes is evaluated by the so-called improvement factor (IF), which is defined as the ratio of the SINR of output to the SNR of input. If we assume the SNR of input to be 1 (0dB), then IF will be identical to SINR of output as given by Equation (22). Both the IF and SINR are used interchangeably in this report. Figure 6 shows the SINR of the optimum processor given by Equation (22) when the antenna looks at the broadside. It can be seen that the coherent processing gain achieves the upper limit of the system (in our case, it is $10\log_{10}(18\times 18) = 25.1$ dB) except around the Doppler frequency of 0 Hz, where the filter notches the clutter.

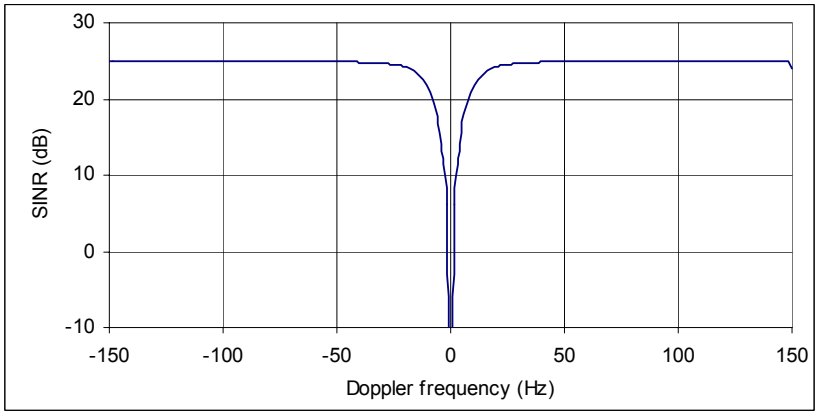

Figure 6: SINR of the fully adaptive STAP when the antenna looks at the broadside.

The response of the weight vector to the angle and Doppler is referred to as the adapted pattern and defined by (Ward, 1994),

$$P_w = \left|\mathbf{w}^H \mathbf{v}(\vartheta, \varpi)\right|^2 \tag{23}$$

Figure 7 shows an adapted pattern for the optimum STAP. The assumed target is at the broadside (90^o azimuth) with a Doppler frequency of 100 Hz and has a SNR of 0dB at the input. The clutter and jamming signals are above the noise 47dB (CNR) and 38dB (JNR), respectively. It can be seen that clutter (the diagonal ridge) and jamming (two constant azimuth ridges) have been well suppressed. Two principal cuts at the target azimuth and Doppler are shown in Figure 8.

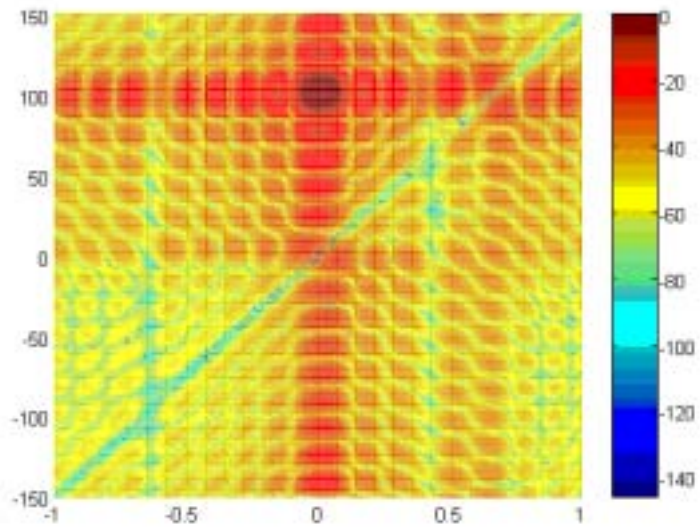

Figure 7: Adaptive pattern of the optimum processor. The horizontal abscissa is cosine of azimuth angle and the vertical abscissa the Doppler frequency.

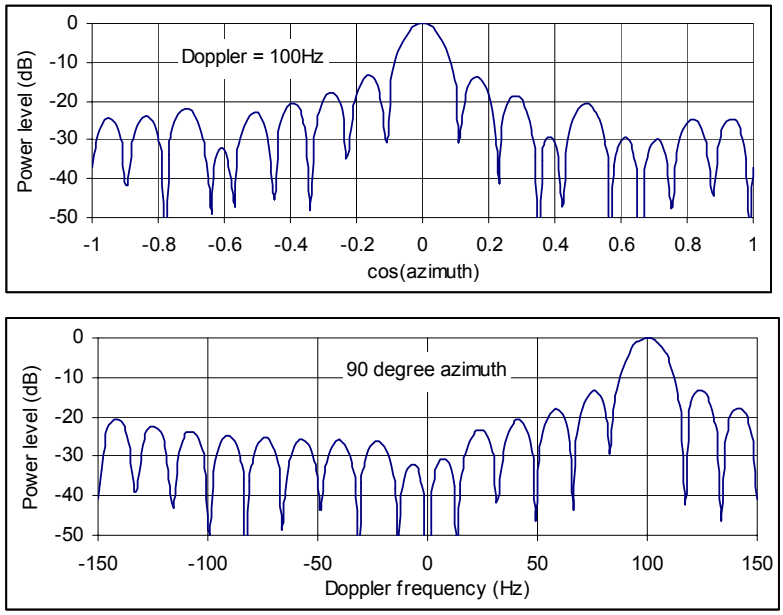

Figure 8: Principal cuts of the adapted pattern at the target azimuth and Doppler.

3.2 Partially Adaptive STAP

Fully adaptive STAP given in Section 3.1 is optimum for detecting desired target signals embedded in interference and noise signals. To implement the fully adaptive STAP in real-time, however, the CM with dimensions of $MN \times MN$ is often too large to be inverted in the

available time. In addition a large dimensionality also requires a large number of identically independent distribution (iid) samples to compute the ensemble average of the CM. The sample matrix inversion (SMI) method requires at least $2MN$ samples to obtain a reliable ensemble average of the CM (Reed, et al, 1974), which is often impractical.

As discussed, the CM has a Toeplitz-block-Toeplitz pattern and it is also Hermitian. Figure 9 depicts the pattern of $\mathbf{R}_u$ assuming $M = 4$. Each small block denotes a $N \times N$ matrix. The Toeplitz-block-Toeplitz pattern means that each $N \times N$ matrix itself is Toeplitz and all diagonal matrix blocks are identical. Since the matrix is Hermitian, the total number of different elements[1] in the whole matrix includes:

- N elements in main diagonal blocks, and
- $(2N-1)(M-1)$ elements in remaining diagonal blocks.

Therefore the information presented in the CM is highly repetitive, which mathematically provides a base for possible reductions in the dimensionality of the matrix with little loss of IF.

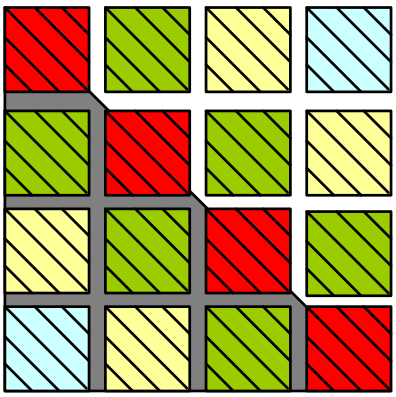

Figure 9: Covariance matrix has a Toeplitz-block-Toeplitz pattern, and it is also Hermitian.

In practice, the reduction of the dimensionality can be realised in the temporal domain by processing a sub-CPI (a few pulses) at a time and/or in the spatial domain by beamforming[2]. Compared to the fully adaptive STAP (no dimensionality reduction), the process with the reduced dimensionality is commonly referred to as partially adaptive STAP or sub-space STAP, which can normally greatly reduce the total computational cost with little loss of IF.

Numerous algorithms have been published in the area of partially adaptive STAP aiming at reducing computation cost. Based on the domains in which the reduced dimensionality applies, these algorithms may be grouped into four categories (Ward 1994, Ward and Kogon, 2004)

[1] The element value might differ from the others in this context.
[2] Beamforming in this context is a spatial-only operation.

- Element-space pre-Doppler;
- Element-space post-Doppler;
- Beam-space pre-Doppler; and
- Beam-space post-Doppler.

The element-space pre-Doppler algorithm uses K_t pulses (usually 2 or 3) at a time, and applies the familiar 2 or 3 pulse clutter canceller principle to suppress clutter. The adaptive process is then applied to a reduced dimension of $K_t N$ instead of a full dimension of MN. Depending on whether the Doppler filtering is applied prior or posterior to space processing, the algorithm is referred to as element-space pre- or post-Doppler. In the later category, in order to make the Doppler processing adaptive, usually two or more Doppler filters have to be adaptively combined for each element.

The dimensionality can be further reduced by beamforming prior to adaptation. The reduction hence can undergo two ways. First the element data is processed with beamforming to produce a small number K_s of beam outputs, and second only K_t pulses are adaptively processed at a time, so the adaptive problem dimensionality becomes $K_s K_t$. Similarly the Doppler processing can be combined with this beam-space architecture in a prior or posterior manner. A universal beamformer matrix is difficult to form in the presence of jamming, if the direction of the jamming is unknown a priori. A typical way is to filter the jamming signals before implementing the beam-space architecture.

Typical algorithms of these four categories have been discussed in detail (Ward, 1994). We only briefly present simulation results here for comparison purposes. Figure 10 to Figure 13 show the performance of four categories of the partially adaptive STAP algorithms in a comparison with the fully adaptive STAP algorithm. It can be seen that for the given conditions, all four partially adaptive STAP algorithms perform similarly, and their SINRs approach the optimum SINR. The ripples in the SINRs are due to the straddling loss of the Doppler filters. In the simulation, the number of Doppler filters used was equal to the number of pulses in a CPI, which is 18.

The necessary condition for partially adaptive STAP to have little IF loss is that the CM must be of strict Toeplitz-block-Toeplitz form. This is the basic assumption in deriving the various partially adaptive STAP algorithms. Therefore, if the measured CM is not strict Toeplitz-block-Toplitz, the partially adaptive STAP may have much lower gains than expected depending upon the degree of the departure from a Toeplitz-block-Toeplitz structure.

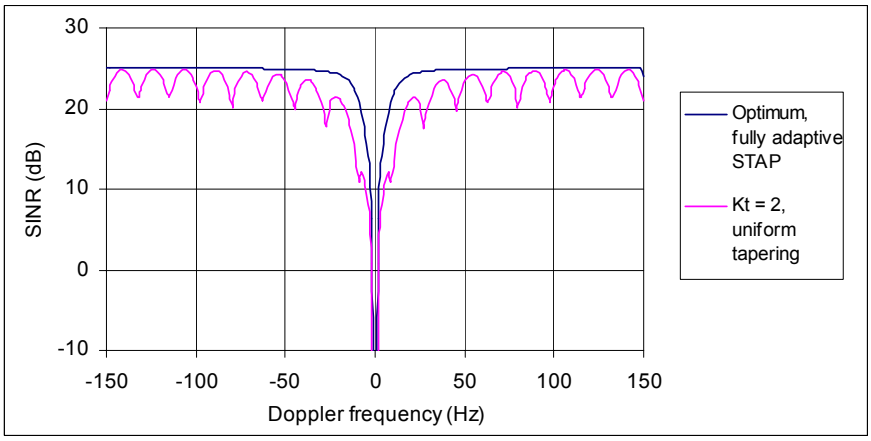

Figure 10: Performance of element-space pre-Doppler algorithm in comparison with that of the fully adaptive STAP.

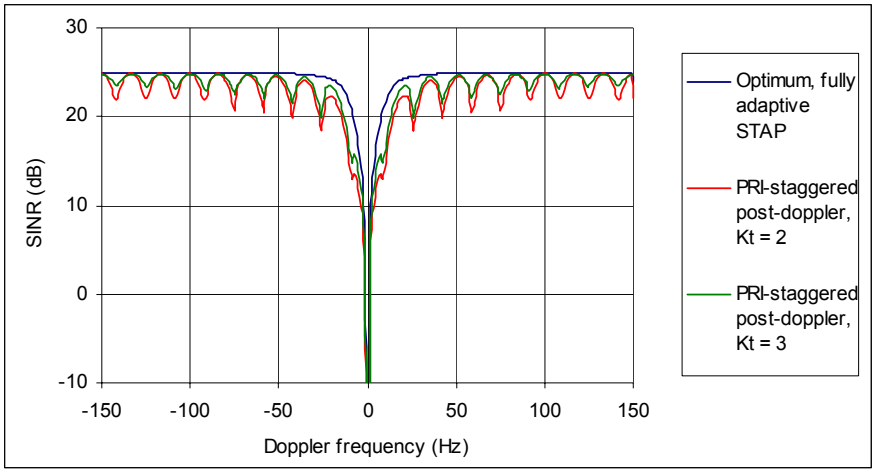

Figure 11: Performance of element-space post-Doppler algorithm in comparison with that of the fully adaptive STAP.

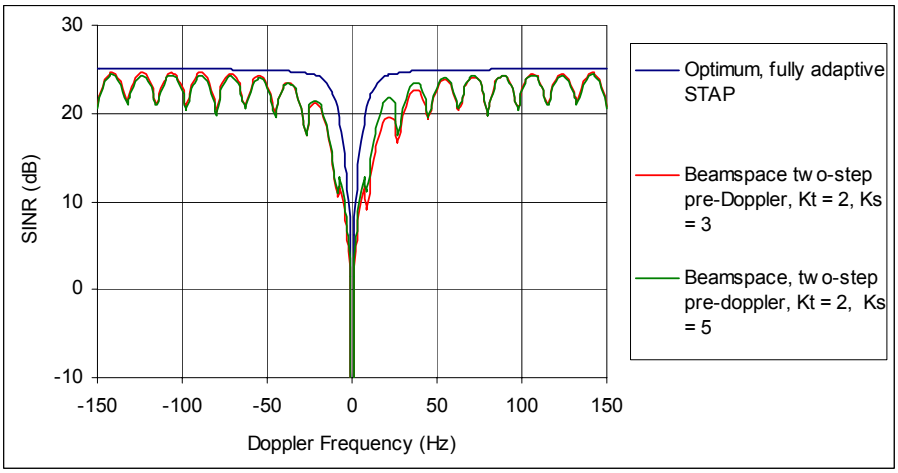

Figure 12: Performance of two-stage beam-space pre-Doppler algorithm in comparison with that of the fully adaptive STAP.

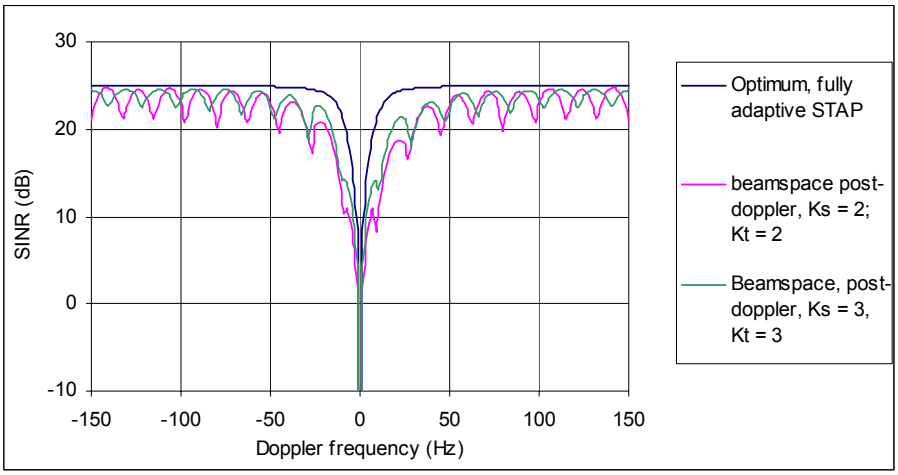

Figure 13: Performance of two-stage beam-space post-Doppler algorithm in comparison with that of the fully adaptive STAP.

4. Approximate Invariance of the Inverse of the Covariance Matrix

Because the optimum processing given in Equation (20) only requires knowledge of the ICM, we are more interested in the characteristics of the ICM rather than the CM itself. In this Section we give two Theorems in support of a claim that the ICM is approximately invariant, based on which, a concept of PSTAP is proposed.

Mathematically we know that any changes in a matrix normally introduce changes in its inverse. However because of its structure it is possible that $\mathbf{R}_u$ can vary in such a way that the resultant variations in $\mathbf{R}_u^{-1}$ are ignorable. The following two Theorems specify the changes in $\mathbf{R}_u$ which introduce ignorable changes in $\mathbf{R}_u^{-1}$.

It is useful to introduce the matrix inversion lemma before introducing two Theorems.

Matrix Inversion Lemma: *Let* $\mathbf{A}$ *and* $\mathbf{C}$ *be square and invertible matrices but need not to be of the same dimension, and* $\mathbf{B}$ *matrix have appropriate numbers of rows and columns, then we have* (Mardia et al, 1979, Wirth, 2001 and Ward, 1994),

$$\left(\mathbf{A}+\mathbf{BCB}^H\right)^{-1} = \mathbf{A}^{-1} - \mathbf{A}^{-1}\mathbf{B}\left(\mathbf{B}^H\mathbf{A}^{-1}\mathbf{B}+\mathbf{C}^{-1}\right)^{-1}\mathbf{B}^H\mathbf{A}^{-1} \tag{24}$$

It is also useful to note a matrix proposition.

Proposition: *The trace of a matrix, ie, the sum of the elements on the main diagonal, is equal to the sum of all eigenvalues of the matrix* (Bodewig, 1959),

$$trace(\mathbf{A}) = \sum_{\lambda_i \in \mathbf{A}} \lambda_i \tag{25}$$

With the assistance Equation (24) and Equation (25), we give the following two theorems.

4.1 Theorem 1

Let the covariance matrix of the undesired signals be the sum of the covariance matrices of clutter, jamming and thermal noise,

$$\mathbf{R}_u = \mathbf{R}_c + \mathbf{R}_j + \mathbf{R}_n \tag{17}$$

where $\mathbf{R}_n = \sigma^2\mathbf{I}$ *and* $\mathbf{R}_c$ *is expressed as,*

$$\mathbf{R}_c = \mathbf{V}\boldsymbol{\Sigma}_c\mathbf{V}^H \tag{8}$$

$\mathbf{V}$ contains N_c space-time steering vectors, $\mathbf{V} = [\mathbf{v}_1 \quad \mathbf{v}_2 \quad \cdots \quad \mathbf{v}_{N_c}]$, and each $\mathbf{v}_k$ $(k = 1, 2, \cdots, N_c)$ is a $MN \times 1$ vector. $\boldsymbol{\Sigma}_c = \sigma^2 \operatorname{diag}([\xi_1 \quad \xi_2 \quad \cdots \quad \xi_{N_c}])$ $(\xi_k > 0, k = 1, 2, \cdots, N_c)$ contains the mean clutter power measured from N_c patches by the receiver. The diagonal elements of $\boldsymbol{\Sigma}_c$ can be divided into two groups, one for those illuminated and received by frontlobes of the transmit and receive antennas, which are assumed to be much greater than the thermal noise, and the other for those illuminated and received by backlobes, which are assumed to be close to zero.

If $\mathbf{R}_j$, $\mathbf{R}_n$ and $\mathbf{V}$ remain unchanged, then $\mathbf{R}_u^{-1}$ remains approximately invariant irrespective of changes in $\boldsymbol{\Sigma}_c$.

Proof

The proof has two steps. First the proof is given for the case without the presence of jamming. The proof for the case with jamming then follows.

Because $\mathbf{v}_k$ $(k = 1, 2, \cdots, N_c)$ is a steering vector, so $\mathbf{v}_k^H \mathbf{v}_k = MN$ (MN is the dimension of $\mathbf{R}_c$). We normalise $\mathbf{V}$ and express $\mathbf{R}_c$ as,

$$\mathbf{R}_c = \mathbf{V}_0 \boldsymbol{\Sigma}_0 \mathbf{V}_0^H \tag{26}$$

where $\mathbf{V}_0 = \mathbf{V} / \sqrt{NM}$ is the normalised steering vector matrix, and $\boldsymbol{\Sigma}_0 = MN\boldsymbol{\Sigma}_c$.

Applying the matrix inversion lemma to the sum of the clutter and noise covariance matrices, $\mathbf{A} = \mathbf{R}_n + \mathbf{R}_c = \sigma^2 \mathbf{I} + \mathbf{V}_0 \boldsymbol{\Sigma}_0 \mathbf{V}_0^H$, we have

$$\mathbf{A}^{-1} = \left(\sigma^2 \mathbf{I} + \mathbf{R}_c\right)^{-1} = \frac{1}{\sigma^2}\mathbf{I} - \frac{1}{\sigma^4}\mathbf{V}_0 \left(\frac{1}{\sigma^2}\mathbf{V}_0^H \mathbf{V}_0 + \boldsymbol{\Sigma}_0{}^{-1}\right)^{-1} \mathbf{V}_0^H \tag{27}$$

The clutter values are only relevant to the diagonal elements of $\left(\frac{1}{\sigma^2}\mathbf{V}_0^H \mathbf{V}_0 + \boldsymbol{\Sigma}_0{}^{-1}\right)$, but with the condition of the theorem, for the clutter patches measured by frontlobes, the diagonal elements simplify to,

$$\frac{1}{\sigma^2} + \frac{1}{MN\sigma^2 \xi_k} \approx \frac{1}{\sigma^2} \quad (\text{as } \xi_k >> 1) \tag{28}$$

whereas for the clutter patches measured by backlobes, the diagonal elements simplify to,

$$\frac{1}{\sigma^2}+\frac{1}{MN\sigma^2\xi_k}=M_0\to\infty \qquad (\text{as } \xi_k\approx 0\text{, see note [3]}) \tag{29}$$

From Equations (28) and (29) we can see that since expressions for the diagonal elements of $\left(\frac{1}{\sigma^2}\mathbf{V}^H\mathbf{V}+\boldsymbol{\Sigma}_0^{-1}\right)$ are approximately independent to specific clutter values ξ_i ($i=1,2,\cdots,N_c$), all elements of $\mathbf{A}^{-1}$ should also be approximately independent to specific clutter values ξ_i in $\boldsymbol{\Sigma}_c$.

With the presence of jamming,

$$\mathbf{R}_u=\mathbf{A}+\mathbf{R}_j \tag{30}$$

Applying the matrix inversion lemma to Equation (30), because $\mathbf{A}^{-1}$ is approximately invariant to changes in $\boldsymbol{\Sigma}_c$, we immediately deduce that $\mathbf{R}_u^{-1}$ is also approximately invariant to changes in $\boldsymbol{\Sigma}_c$. The proof is complete.

Rigorously speaking, the above proof is only approximately and qualitatively. It is difficult to quantitatively indicate how $\mathbf{R}_u^{-1}$ is invariant to the changes in $\boldsymbol{\Sigma}_c$, and give the error analysis for the ICM. Therefore we present several numerical examples below to verify Theorem 1, and demonstrate that $\mathbf{R}_u^{-1}$ is invariant to variations that are likely to be observed in practice.

4.1.1 Example 1

The clutter pattern received from a ring at *R = 130 km*, assuming the clutter coefficient $\sigma_0(\theta,\phi_k)$, $k=1,\cdots,N_c$, to be constant, is shown in Figure 2. We denote this as clutter pattern case 1 for convenience. The corresponding clutter power component in $\boldsymbol{\Sigma}_c$ is denoted as $\xi_{k(1)}$ ($k=1,\cdots,N_c$). Now assume the mean clutter power $\xi_{i(1)}$ to undergo a random variation as,

$$\xi_{k(2)}=100\left|randn()\right|\xi_{k(1)} \qquad k=1,\cdots,N_c \tag{31}$$

---

[3] Because $\mathbf{R}_u^{-1}$ exists, so all its elements are finite. To express the relationship between an element of $\mathbf{R}_u^{-1}$ and M_0, in general, it can be considered as a ratio of two polynomial functions of M_0 as $\frac{a_nM_0^n+a_{n-1}M_0^{n-1}+\cdots+a_0}{b_mM_0^m+b_{m-1}M_0^{m-1}+\cdots+b_0}$, with $m\ge n$. There are three possible results of the ratio: (1) $=a_0/b_0$ if $m=n=0$; (2) $\approx a_n/b_n$, if $m=n$; and (3) ≈ 0 if $m>n$.

where $randn()$ is the $(0,1)$ Gaussian random function. The resultant clutter pattern will be a random pattern, with most measures $\xi_{k(2)}$ higher than $\xi_{k(1)}$ by 0 to 20dB (corresponding to the $|randn()|$ function varying in the range of $(0.01,1)$). We denote this clutter pattern as case 2. The clutter pattern comparison between case 1 and case 2 is shown in Figure 14. Clutter pattern case 1 may simulate returns from a homogeneous surface, such as bare soil, as $\sigma_0(\theta,\phi_k)$, $k=1,\cdots,N_c$, is assumed to be constant. In contrast, clutter pattern case 2 may simulate returns from inhomogeneous forests, as the majority returns are 0 to 20dB randomly higher than that of case 1.

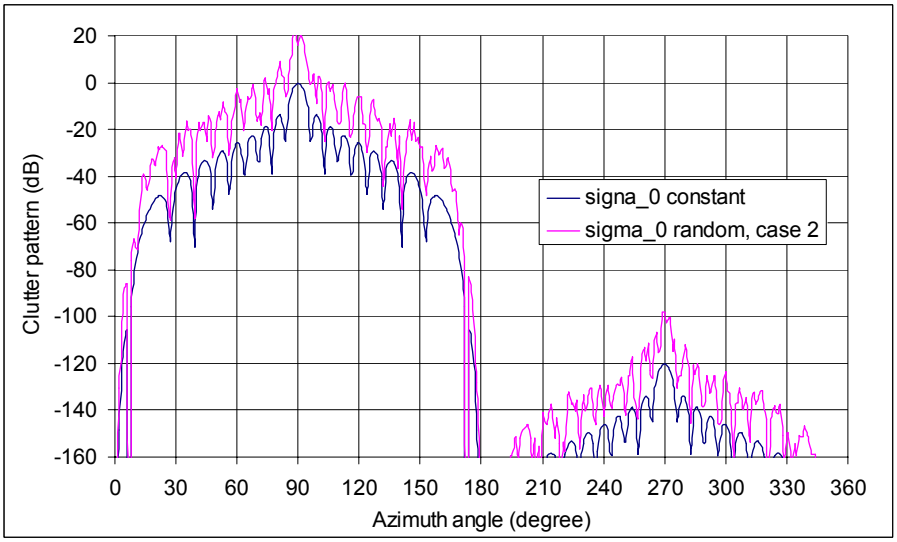

Figure 14: Clutter pattern comparison of case 1 and case 2.

With the usual assumption of $\mathbf{R}_j$, $\mathbf{R}_n$ and $\mathbf{V}$ remaining unchanged, all 324-by-324 elements of $\mathbf{R}_u$ and $\mathbf{R}_u^{-1}$ for clutter pattern case 1, and case 2, respectively, are numerically compared. The one-one plot of the element-to-element comparison (real and imaginary parts separately) for the two CMs is shown in Figure 15, and little correlation between the two CMs is observed. Because the CM is Hermitian and has a Toeplitz-block-Toeplitz pattern, it only has $N+(2N-1)(M-1)=613$ elements whose values might differ from others at the most. This is why there are not many circles shown in Figure 15 (many are overlapped). On the other hand, the element-to-element comparison for the two ICMs is shown in Figure 16. The comparison indicates that the two ICMs, from the engineering point of view, are almost identical, and the differences are so small and insignificant that they can be ignored.

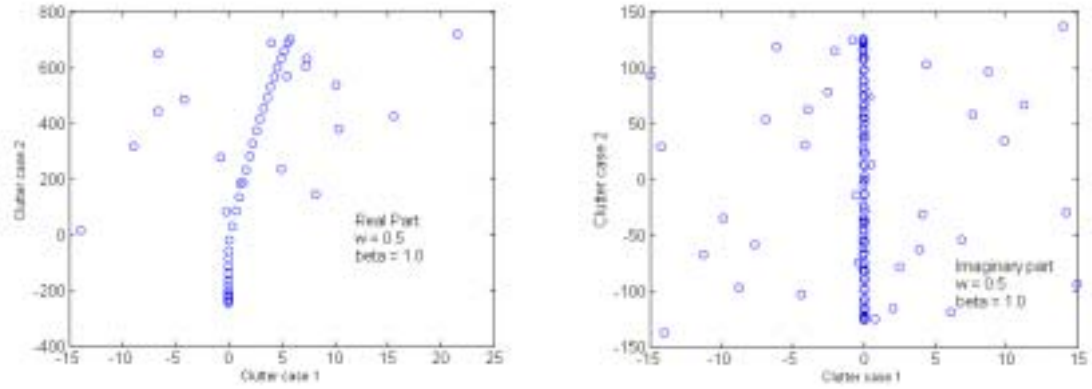

(a) Real part (b) Imaginary part

Figure 15: Element-to-element comparison of the two covariance matrices for clutter case 1 and case 2. Little correlation between the two covariance matrices is observed (note the scale differences in abscissas).

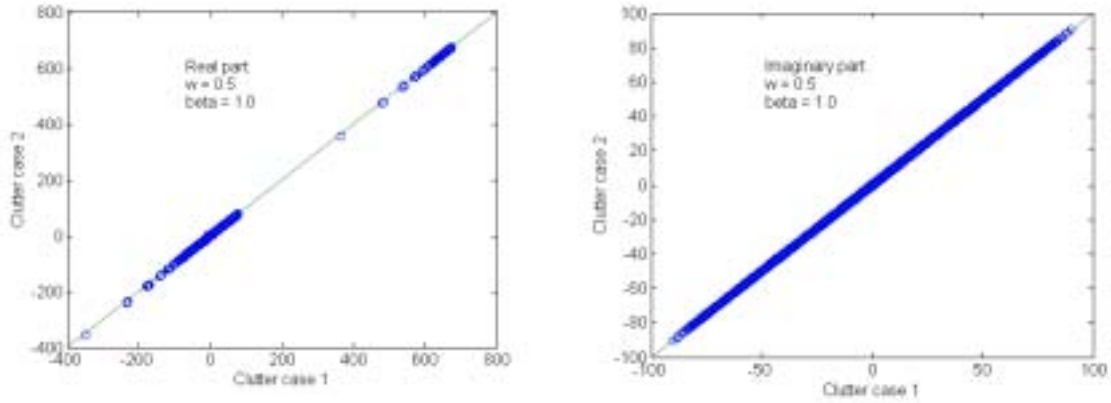

(a) Real part (b) Imaginary part

Figure 16: Element-to-element comparison of the two inverses of the covariance matrices for clutter case 1 and case 2.

4.1.2 Example 2

In this example clutter pattern case 3 is defined as,

$$\xi_{k(3)} = 10^{15\,randn()/10}\,\xi_{k(1)} \qquad k = 1,\cdots,N_c \tag{32}$$

The resultant clutter pattern will be random, with most measures $\xi_{k(3)}$ varying around $\xi_{k(1)}$ by ± 15 dB (corresponding to the $randn()$ function varying in the range of $(-1,1)$). The clutter pattern comparison between case 1 and case 3 is shown in Figure 17. Clutter case 3

may be considered as an extreme example of variation in clutter as measured clutter patterns are most unlikely to be worse than this.

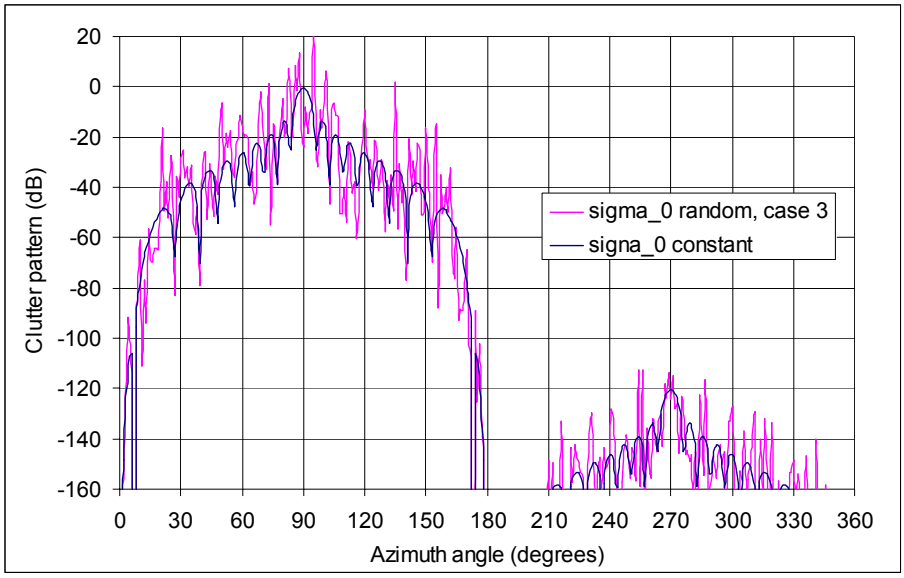

Figure 17: Clutter pattern comparison of case 1 and case 3.

With the usual assumption of $\mathbf{R}_j$, $\mathbf{R}_n$ and $\mathbf{V}$ remaining unchanged, the element-to-element comparison (real and imaginary parts separately) for all 324-by-324 elements of $\mathbf{R}_u^{-1}$ for clutter case 1, and case 3 is plotted in Figure 18. Again, no significant differences are found.

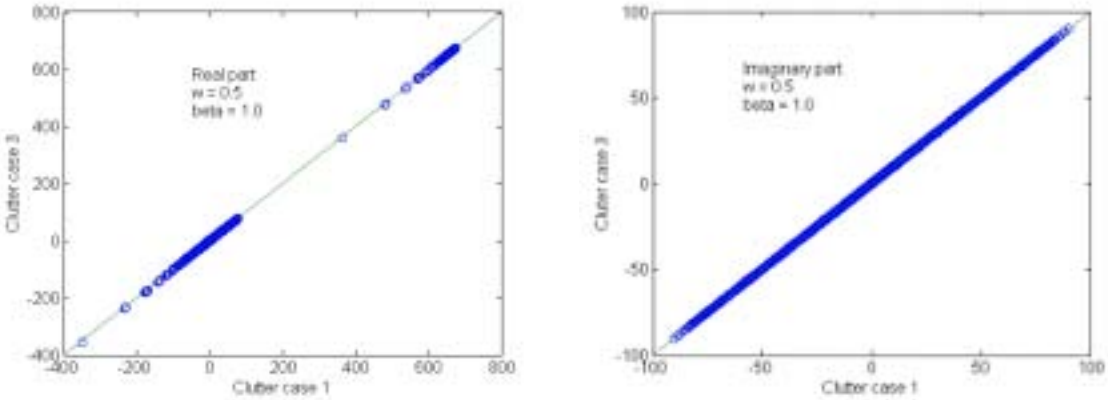

(a) Real part (b) Imaginary part

Figure 18: Element-to-element comparison of the two inverses of the covariance matrices for clutter case 1 and case 3.

4.1.3 Examples 3, 4 and 5

Each of the following comparisons is with the usual assumption of $\mathbf{R}_j$, $\mathbf{R}_n$ and $\mathbf{V}$ remaining unchanged.

Example 3 considers a scenario in which the antenna is steered 40^o from the broadside, and the clutter pattern follows case 3 but with a random variation of only ± 10 dB. The clutter pattern comparison is shown in Figure 19. The element-to-element comparison for the two ICMs is shown in Figure 20.

Examples 4 and 5 consider scenarios in which the antenna element interval is not a half-wavelength, and the clutter fold-over β is not equal to 1. In particular, Example 4 compares clutter pattern case 1 to case 3 (random ± 10 dB) with $d/\lambda = 0.4$ and $\beta = 0.8$, while Example 5 compares clutter pattern case 1 and case 3 (random ± 10 dB) with $d/\lambda = 0.5$ and $\beta = 1.2$. The element-to-element comparisons for the two ICMs for Examples 4 and 5 are shown in Figure 21 and Figure 22, respectively. It can be seen that element differences increases for both examples, but overall, the linear correlation is still very high.

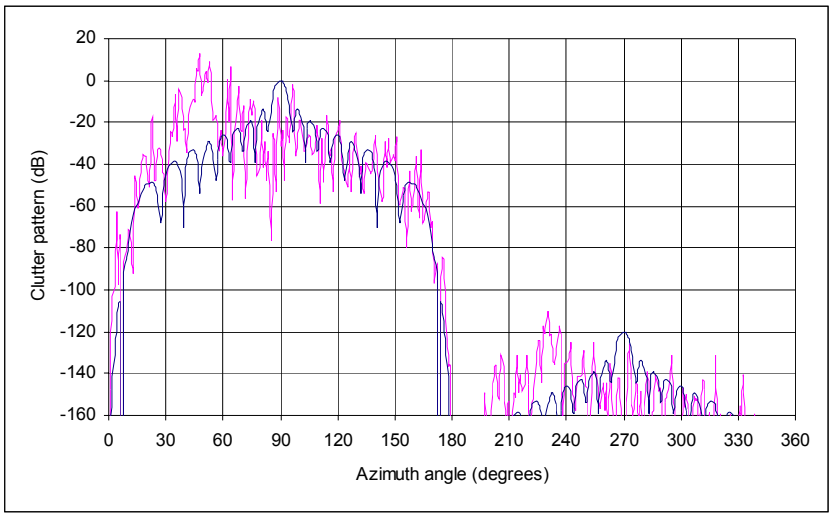

Figure 19: Clutter pattern comparison of case 1 and case 3. In case 3, not only is the clutter random, but the antenna is also steered 40^o from the broadside (mainlobe points to 50^o azimuth).

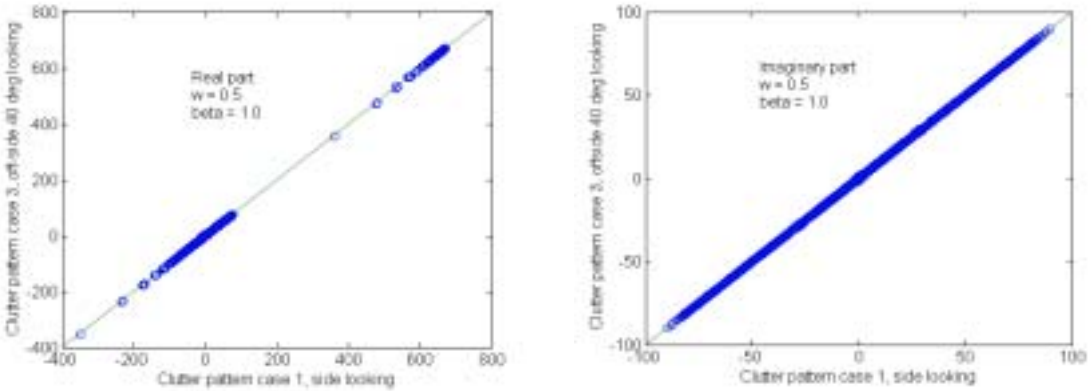

(a) Real part (b) Imaginary part

Figure 20: Element-to-element comparison of two inverses of the covariance matrices for clutter case 1 and case 3 with antenna steered 40° from broadside.

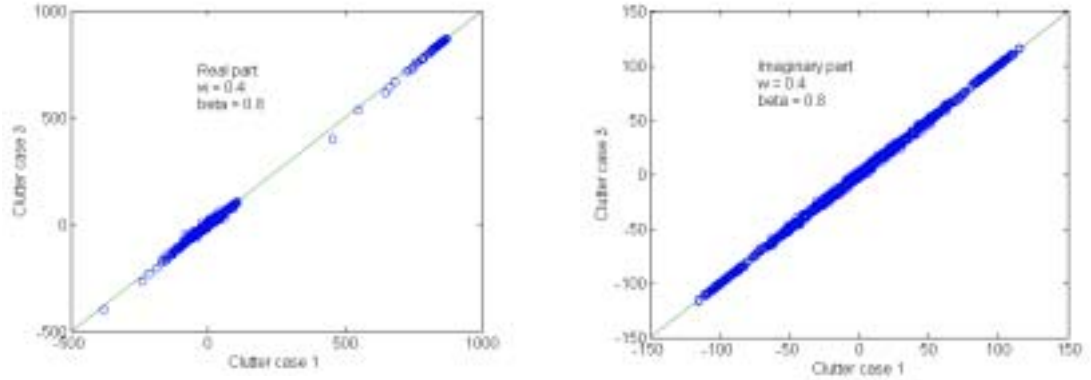

(a) Real part (b) Imaginary part

Figure 21: Element-to-element comparison of two inverses of the covariance matrices for clutter case 1 and case 3 with $d/\lambda = 0.4$ *and* $\beta = 0.8$.

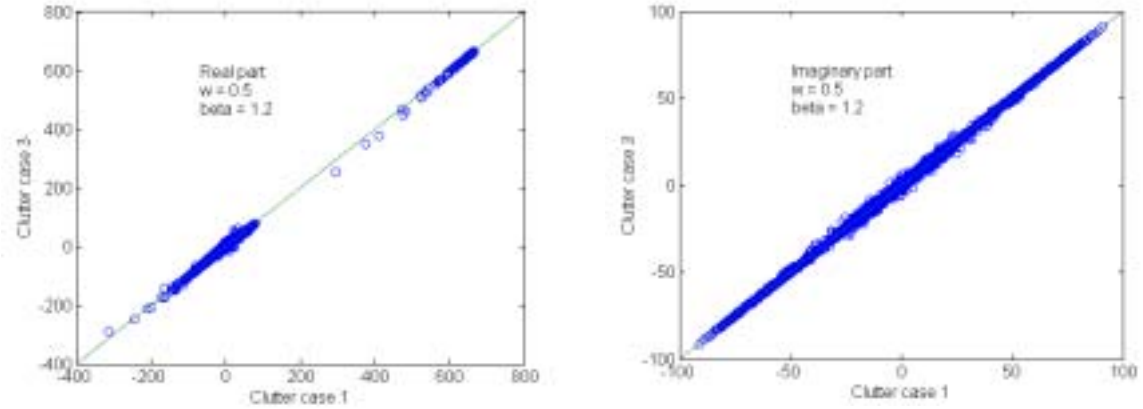

(a) Real part (b) Imaginary part

Figure 22: Element-to-element comparison of two inverses of the covariance matrices for clutter case 1 and case 3 with $d/\lambda = 0.5$ *and* $\beta = 1.2$.

The familiar statistical parameter, the correlation coefficient, r^2, usually measures the linear correlation between two vectors, $\mathbf{x}$ and $\mathbf{y}$, with the same length. The correlation coefficient, r^2, is defined as

$$r^2 = \frac{\left[n\sum_{i=1}^{n} x_i y_i - \left(\sum_{i=1}^{n} x_i\right)\left(\sum_{i=1}^{n} y_i\right)\right]^2}{\left[\left(n\sum_{i=1}^{n} x_i^2 - \left(\sum_{i=1}^{n} x_i\right)^2\right)\left(n\sum_{i=1}^{n} y_i^2 - \left(\sum_{i=1}^{n} y_i\right)^2\right)\right]} \tag{33}$$

The linear correlation between two ICMs (each ICM is stacked as a vector) may be measured using the same parameter, r^2. Table 1 lists the values of r^2 for the examples we have used. It can be seen that even for the worst case of Example 5, the values of r^2 are still as high as 0.9982 and 0.9983 for the real part and the imaginary part, respectively.

Table 1: Statistical measure r^2 *for the five examples.*

Example	Correlation coefficient r^2	
	Real part	Imaginary part
Example 1	0.9996	0.9999
Example 2	0.9996	0.9999
Example 3	0.9996	0.9999
Example 4	0.9990	0.9980
Example 5	0.9982	0.9983

4.2 Theorem 2

Let the covariance matrix of the undesired signals be the sum of the covariance matrices of clutter, jamming and thermal noise,

$$\mathbf{R}_u = \mathbf{R}_c + \mathbf{R}_j + \mathbf{R}_n \tag{17}$$

where $\mathbf{R}_n = \sigma^2\mathbf{I}$. $\mathbf{R}_c$ *and* $\mathbf{R}_j$ *are positive semi-definite but low rank matrices. Let* $rank(\mathbf{R}_c) = r_c$, $rank(\mathbf{R}_j) = r_j$, λ_c *and* λ_j *be the smallest of the non-zero eigenvalues of* $\mathbf{R}_c$ *and* $\mathbf{R}_j$, *respectively.*

Suppose that $\mathbf{R}_u$ *undergoes a change as,*

$$\mathbf{R}_{u'} = k_c\mathbf{R}_c + k_j\mathbf{R}_j + k_n\mathbf{R}_n \tag{34}$$

If $\lambda_c >> \sigma^2$, $\lambda_j >> \sigma^2$, *and* k_c, k_j *and* k_n *are real and positive scalars whose values satisfy the conditions* $k_c\lambda_c >> k_n\sigma^2$ *and* $k_j\lambda_j >> k_n\sigma^2$, *then*

$$\mathbf{R}_{u'}^{-1} \approx \frac{1}{k_n}\mathbf{R}_u^{-1} \tag{35}$$

The condition of $\lambda_c >> \sigma^2$ and $\lambda_j >> \sigma^2$ is generally true as clutter and jamming are much stronger than the thermal noise. Now let us prove Theorem 2.

Proof

For simplicity, first consider a covariance matrix comprising two components,

$$\mathbf{R}_u = \mathbf{R}_n + \mathbf{R}_c = \sigma^2\mathbf{I} + \mathbf{R}_c \tag{36}$$

According to the matrix inversion lemma, we have,

$$\mathbf{R}_u^{-1} = \left(\sigma^2\mathbf{I} + \mathbf{R}_c\right)^{-1} = \left(\sigma^2\mathbf{I} + \mathbf{E}\mathbf{\Lambda}\mathbf{E}^H\right)^{-1} = \frac{1}{\sigma^2}\mathbf{I} - \frac{1}{\sigma^4}\mathbf{E}\left(\frac{1}{\sigma^2}\mathbf{E}^H\mathbf{E} + \mathbf{\Lambda}^{-1}\right)^{-1}\mathbf{E}^H \tag{37}$$

where $\mathbf{R}_c$ is expressed by its eigenvector decomposition as $\mathbf{R}_c = \mathbf{E}\mathbf{\Lambda}\mathbf{E}^H$ (note $\mathbf{\Lambda}_c$ is a $r_c \times r_c$ diagonal matrix).

Now letting $k_c = 1$ and $k_n = k$, we have

$$\mathbf{R}_{u'} = k\,\mathbf{R}_n + \mathbf{R}_c = k\sigma^2\mathbf{I} + \mathbf{R}_c \tag{38}$$

$$k\,\mathbf{R}_{u'}^{-1} = k\left(k\sigma^2\mathbf{I}+\mathbf{R}_c\right)^{-1} = k\left[\frac{1}{k\sigma^2}\mathbf{I}-\frac{1}{k^2\sigma^4}\mathbf{E}\left(\frac{1}{k\sigma^2}\mathbf{E}^H\mathbf{E}+\mathbf{\Lambda}^{-1}\right)^{-1}\mathbf{E}^H\right]$$
$$= \frac{1}{\sigma^2}\mathbf{I}-\frac{1}{\sigma^4}\mathbf{E}\left(\frac{1}{\sigma^2}\mathbf{E}^H\mathbf{E}+k\,\mathbf{\Lambda}^{-1}\right)^{-1}\mathbf{E}^H \tag{39}$$

Comparing Equations (37) and (39), the difference exists only between the corresponding diagonal elements of $\left(\frac{1}{\sigma^2}\mathbf{E}^H\mathbf{E}+\mathbf{\Lambda}^{-1}\right)$ and $\left(\frac{1}{\sigma^2}\mathbf{E}^H\mathbf{E}+k\,\mathbf{\Lambda}^{-1}\right)$. Also the diagonal elements of $\mathbf{E}^H\mathbf{E}$ are all equal to 1 as $\mathbf{E}$ is the eigenvector matrix of $\mathbf{R}_c$. The i^{th} diagonal elements of $\left(\frac{1}{\sigma^2}\mathbf{E}^H\mathbf{E}+\mathbf{\Lambda}^{-1}\right)$ and $\left(\frac{1}{\sigma^2}\mathbf{E}^H\mathbf{E}+k\,\mathbf{\Lambda}^{-1}\right)$, respectively, are,

$$\frac{1}{\sigma^2}+\frac{1}{\lambda_i} = \frac{\lambda_i+\sigma^2}{\sigma^2\lambda_i} \tag{40}$$

and

$$\frac{1}{\sigma^2}+\frac{k}{\lambda_i} = \frac{\lambda_i+k\sigma^2}{\sigma^2\lambda_i} \tag{41}$$

The assumption of $\lambda_i >> \sigma^2$, $i = 1,2,\cdots,r_c$, results in that both expressions of Equations (40) and (41) approach $1/\sigma^2$. Therefore we have,

$$\mathbf{R}_{u'}^{-1} \approx \frac{1}{k}\mathbf{R}_u^{-1} = \frac{1}{k_n}\mathbf{R}_u^{-1} \tag{42}$$

If $k_c \neq 1$

$$\mathbf{R}_{u''} = k_n\sigma^2\mathbf{I}+k_c\mathbf{R}_c = k_c\left(k\sigma^2\mathbf{I}+\mathbf{R}_c\right) = k_c\mathbf{R}_{u'} \tag{43}$$

where $k = k_n / k_c$. Using the result of Equation (46), we have,

$$\mathbf{R}_{u''}^{-1} = \frac{1}{k_c}\mathbf{R}_{u'}^{-1} \approx \frac{1}{k_c}\frac{k_c}{k_n}\mathbf{R}_u^{-1} = \frac{1}{k_n}\mathbf{R}_u^{-1} \tag{44}$$

In the presence of jamming, we may need to further assume that the smallest non-zero eigenvalue of $(\mathbf{R}_c + \mathbf{R}_j)$ is still much greater than σ^2. This assumption is generally true, by noting,

$$rank(\mathbf{R}_c + \mathbf{R}_j) \le rank(\mathbf{R}_c) + rank(\mathbf{R}_j) \tag{45}$$

and

$$trace(\mathbf{R}_c + \mathbf{R}_j) = trace(\mathbf{R}_c) + trace(\mathbf{R}_j) \tag{46}$$

Therefore the number of non-zero eigenvalues of $(\mathbf{R}_c + \mathbf{R}_j)$ is no more than the total number of the non-zero eigenvalues of $\mathbf{R}_c$ and $\mathbf{R}_j$. On the other hand, the sum of the eigenvalues of $(\mathbf{R}_c + \mathbf{R}_j)$ are equal to the sum of the eigenvalues of $\mathbf{R}_c$ and $\mathbf{R}_j$.

Reorganising (34) as,

$$\mathbf{R}_{u'} = k_c \left[\frac{k_n}{k_c}\sigma^2\mathbf{I} + \left(\mathbf{R}_c + \frac{k_j}{k_c}\mathbf{R}_j \right) \right] \tag{47}$$

let $\mathbf{R}_{c'} = \mathbf{R}_c + \frac{k_j}{k_c}\mathbf{R}_j$, the remaining proof is the same as the proof for Equation (38). The proof is complete.

Similarly, the proof of Theorem 2 is only approximately and qualitatively. Numerical examples are therefore presented below to verify Theorem 2.

4.2.1 Examples

The CMs of clutter case 1, jamming and noise presented in Section 4 are referred to as the original case. Two other cases are considered, as,

Case 1a: $k_c = 50.0$, $k_j = 1.5$, $k_n = 0.5$; and
Case 1b: $k_c = 0.5$, $k_j = 30$, $k_n = 2.0$.

The element-to-element ICM comparisons between the original case and case 1a, as well as between the original case and case 1b are shown in Figure 23. It can be seen from the figure that the two ICMs for each case are highly linearly correlated. The slope of the correlation is equal to $1/k_n$ irrespective of k_c and k_j.

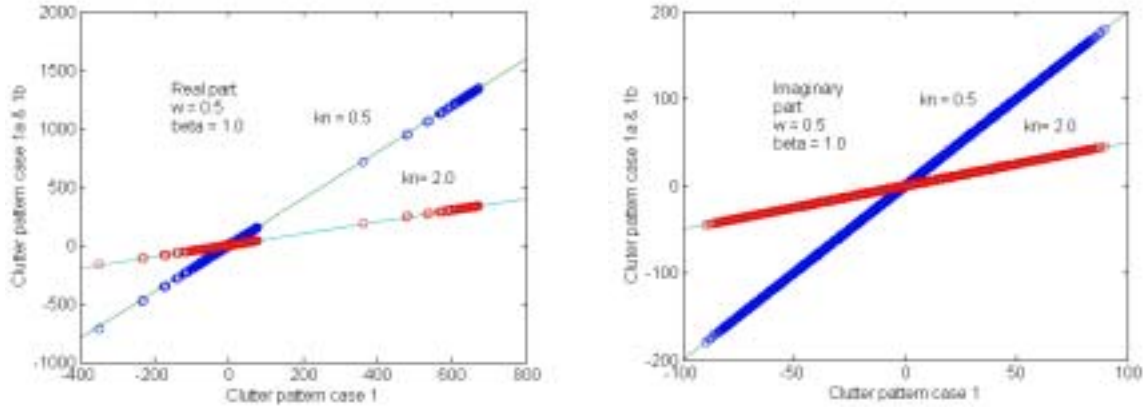

(a) Real part (b) Imaginary part

Figure 23: The linear correlation of the inverses of the covariance matrices. Two cases of $k_c = 50.0$, $k_j = 1.5$ *and* $k_n = 0.5$, *as well as* $k_c = 0.5$, $k_j = 30$ *and* $k_n = 2.0$ *are compared to the original case of* $k_c = k_j = k_n = 1$. *The linear correlation slope is* $1/k_n$ *irrespective of* k_c *and* k_j.

The statistical measure r^2, measuring the linear correlation between the two ICMs (each ICM is stacked as a vector) for the above two cases are given in Table 2.

Table 2: Statistical measure r^2 *for the two cases.*

Case	Correlation coefficient r^2	
	Real part	Imaginary part
Case 1	0.9996	0.9999
Case 2	0.9992	0.9998

4.3 Robust Analysis

The preceding subsection has discussed the invariance of the ICM if the radar and platform parameters remain unchanged. In reality, there always exist uncertainties. For instance, air turbulence could cause variations in drift angle, roll angle and velocity etc for the platform. We assume that all system parameters can be measured at a relatively accurate level, and the effects due to system uncertainties are therefore insignificant and not discussed further. However there still exist other uncertainties beyond our control. A typical uncertainty is that an undulating terrain induces a random variation in the steering angle for the clutter patch. As depicted in Figure 24, for a given range R, surface scatterers within the range resolution $\Delta\rho$ make their clutter contributions to the same range bin. A flat terrain surface corresponds to a constant elevation angle θ for a given range R, whereas an undulating terrain surface introduces a random variation $\Delta\theta$ which in turn introduces a variation to the steering vector defined by (3)-(6). Because the height variation Δh is random from patch to patch for an undulating terrain surface, so is the corresponding $\Delta\theta$. According to the geometry shown in Figure 24, the expression for $\Delta\theta$ is,

$$\Delta\theta \approx \frac{\Delta h}{R\cos\theta} \tag{48}$$

In general, for the same Δh, $\Delta\theta$ has bigger values for shorter ranges. For instance, a variation of $\Delta h = \pm 10km$ [4] corresponds to a variation of $\Delta\theta = \pm 4.4^o$ for $R = 130km$ and $H = 9km$. On the other hand, the same variation of $\Delta h = \pm 10km$ incurs a variation of $\Delta\theta = \pm 11.5^o$ for $R = 50km$ and $H = 5km$.

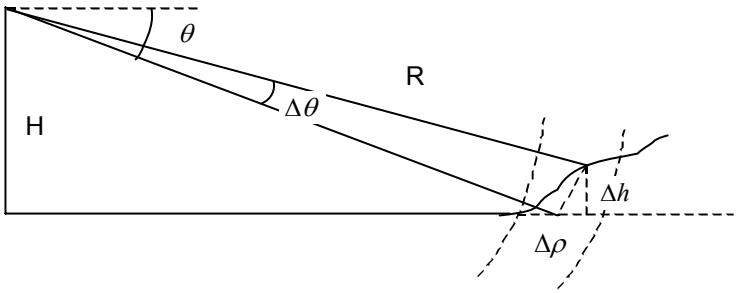

Figure 24: Uncertainty of the steering vector due to an undulating terrain.

Without loss of generality, we define the elevation angle for the k^{th} clutter patch as,

$$\theta_k = \theta + \Delta\theta[2\,rand() - 1] \tag{49}$$

where $rand()$ is a random function with a uniformly distributed interval of $(0,1)$. The corresponding steering angle specified by Equation (6) becomes,

$$\vartheta_k = \frac{d}{\lambda}\cos\theta_k \cos\phi_k \tag{50}$$

A random variation in elevation angle ($\Delta\theta = 10^o$) simulating an undulating terrain is shown in *Figure 25*, in comparison with a constant elevation angle simulating a flat terrain surface with $R = 130km$ and $H = 9km$.

[4] The highest peak of the Himalayas is only 8796m.

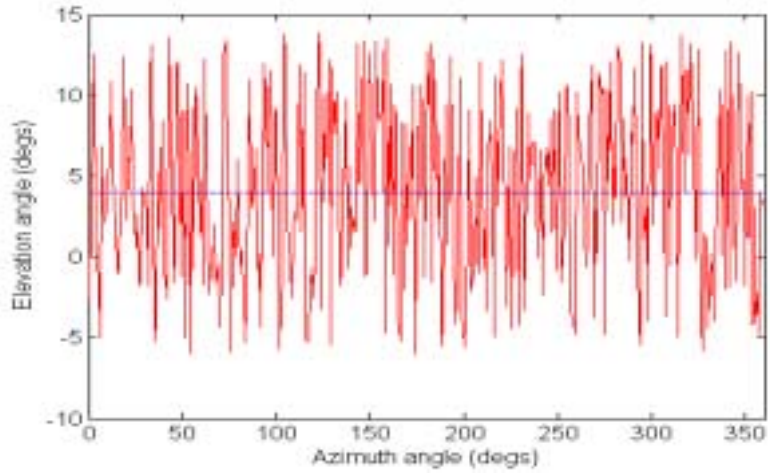

Figure 25: Constant elevation angle for a flat terrain surface versus random elevation angle (a variation of $\pm 10^o$) for an undulating terrain surface.

To examine the effect of an undulating terrain surface on the ICM as well as the IF performance of the PSTAP, the clutter pattern case 3 is again used in comparison with the clutter pattern case 1. However this time for case 3, not only does its intensity randomly vary $\pm 15dB$ as shown in Figure 17, but also its elevation angle randomly varies $\pm 10^o$ as shown in *Figure 25*. This scenario is referred to as clutter case 3a in order to differentiate it from the previously defined case 3. Due to the random variation in elevation angle, elements of the steering matrix $\mathbf{V}$ also alter accordingly, which is shown in Figure 26 where the elements of the steering matrix corresponding to a flat terrain surface are used for the comparison. It can be seen that there is little correlation between the two steering matrices. The element-to-element ICM comparison between case 1 (constant clutter coefficient and constant elevation angle) and case 3a (random clutter coefficient with a variation of $\pm 15dB$ and random elevation angle with a variation of $\pm 10^o$) in Figure 27 shows that the two ICMs are still strongly correlated. Finally the IF of PSTAP (using the optimum weighting vector obtained from clutter case 1 to compute the IF values for clutter case 3a, see (52)) is shown in Figure 28 together with the IF of STAP (using the optimum weighting vector obtained from clutter case 1 to computer the IF values for clutter case 1) for comparison. It clearly shows that even for such a scenario with severely uncertain conditions, PSTAP still possesses a nearly identical IF performance as STAP for the whole Doppler frequency spectrum. The PSTAP SINR loss, compared to the STAP SINR, due to the uncertainties in clutter intensity and steering angle as specified as case 3a, ie, the difference of the two SINR curves in Figure 28, is shown in Figure 29. It can be seen that the SINR loss is insignificant (usually less than 0.2dB) except at the centre frequency of the notch where a significant loss happens. However, the loss at the centre frequency of the notch means that the notch is deeper and has even a greater capability of clutter suppression.

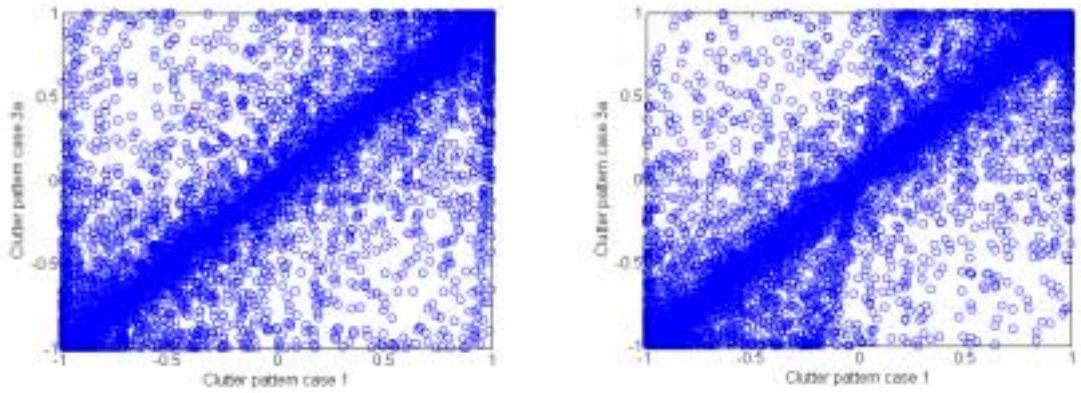

(a) real part (b) imaginary part

Figure 26: Elements of the steering matrix $\mathbf{V}$ *for a randomly undulating terrain surface compared with the corresponding elements for a flat terrain surface.*

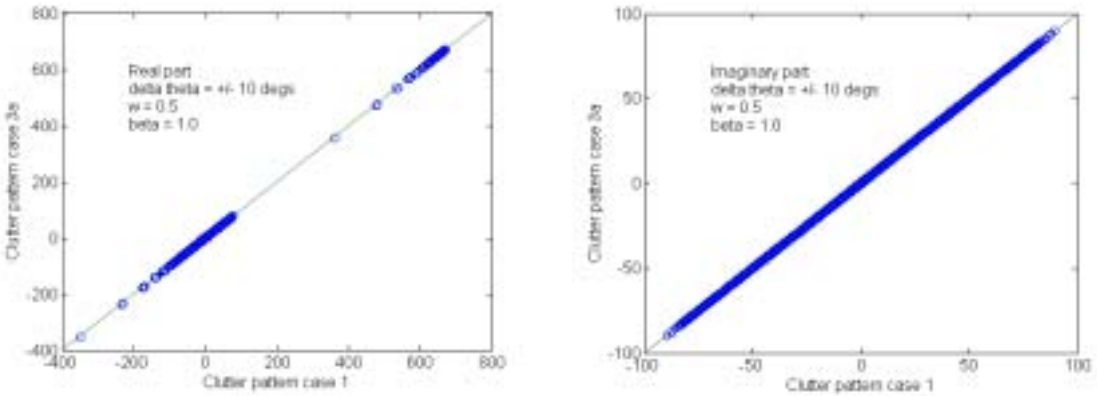

(a) real part (b) imaginary part

Figure 27: Element-to-element ICM comparison between clutter case 1 (constant clutter coefficient and constant elevation angle) and clutter case 3a (random clutter coefficient with a variation of $\pm 15dB$ *and random elevation angle with a variation of* $\pm 10^{o}$ *).*

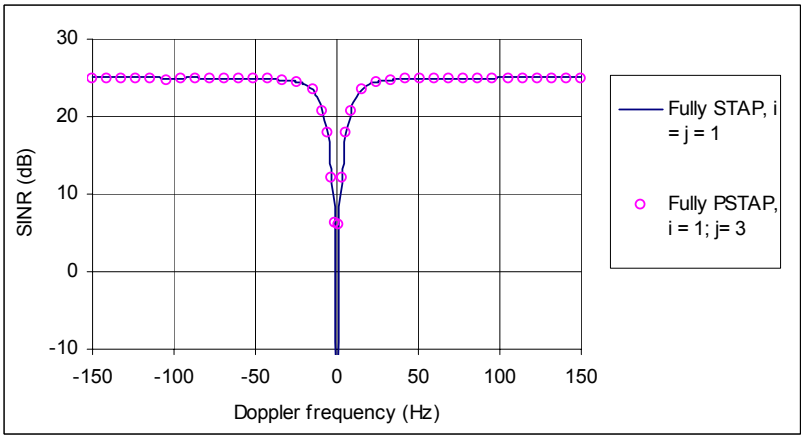

Figure 28 IF values of PSTAP (for clutter case 3a) are nearly identical to that of STAP for the whole Doppler spectrum. The maximum IF loss of PSTAP is about 0.2dB.

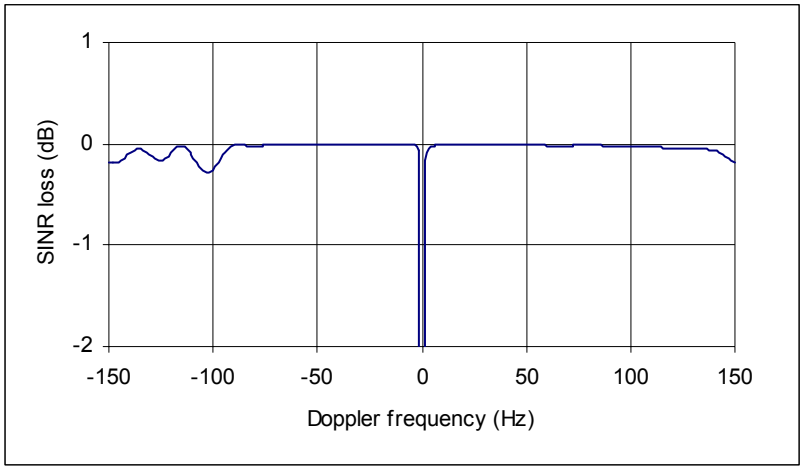

Figure 29: PSTAP SINR loss, compared to the STAP SINR, due to uncertainties in clutter intensity and steering angle as specified in case 3a. The loss is usually less than 0.2dB. A significant loss only happens at the centre frequency indicating that the notch of the PSTAP SINR is even deeper.

The above analysis assumes that the height H of the platform is the mean height of the constant range ring on the terrain surface. If the height H is assumed to be referenced to sea level, then the elevation angle for an undulating terrain surface normally can only vary on one side of the nominal elevation angle. The elevation angle for the k^{th} clutter patch can be written as,

$$\theta_k = \theta + \Delta\theta \, rand() \tag{51}$$

Let $\Delta\theta = 10^o$, the random variation of the elevation angle for an undulating terrain surface is shown in Figure 30 in comparison with the constant elevation angle for a flat terrain surface. We define clutter case 3b as having an intensity variation the same as case 3 as shown in Figure 17 and an elevation angle variation as shown in Figure 30. The scenario is compared to the scenario of clutter pattern case 1 (constant clutter coefficient and constant elevation angle). Again the two ICMs are nearly identical. The IF of PSTAP (using the optimum weighting vector obtained from clutter case 1 to computer the IF values for clutter case 3b, see (52)) is shown in Figure 31 together with the comparison to the IF of the STAP (using the optimum weighting vector obtained from clutter case 1 to computer the IF values for clutter case 1). Again it clearly shows that even for such a scenario with severely uncertain conditions PSTAP still possesses the nearly identical IF performance as STAP for the whole Doppler frequency spectrum.

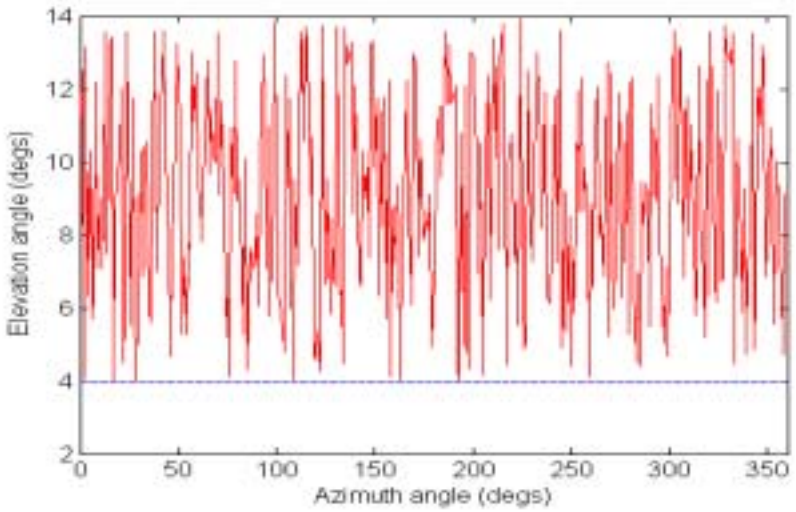

Figure 30: Constant elevation angle for a flat terrain surface versus random elevation angle (a variation of $+10^o$) for an undulating terrain surface.

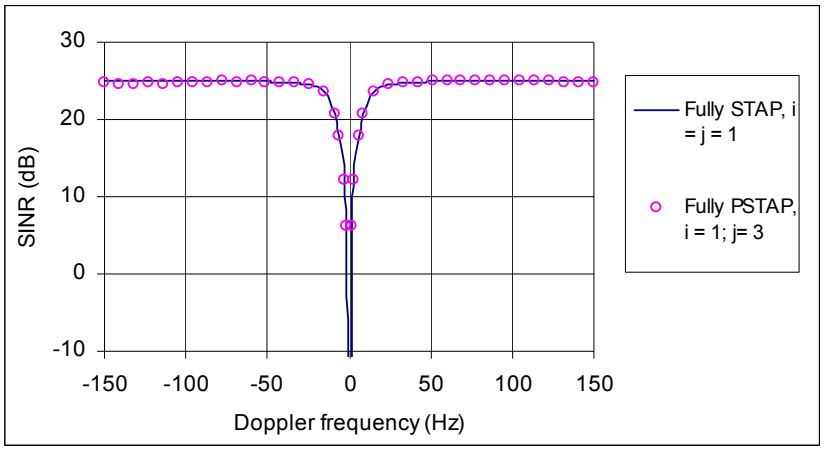

Figure 31: IF values of PSTAP (for clutter case 3b) are nearly identical to that of STAP for the whole Doppler spectrum. The maximum IF loss of PSTAP is about 0.4dB.

Based on the above simulations, it can be concluded that the invariance of the ICM is robust and not sensitive to uncertainties such as random variations in clutter intensities and in elevation angles due to height variations of an undulating terrain surface. This implies that the performance of the PSTAP is stable and suffers little, even used in severely uncertain conditions.

4.4 Significance

The implications of Theorems 1 and 2 are significant. The main points are:

- Theorem 1 indicates that for clutter, adaptive processing needs to adapt only to system parameters (both radar and platform) but not the clutter itself. The fact that the ICM is approximately invariant implies that the ICM is approximately independent of the clutter environment, so that the optimum weighting vectors can be pre-built, as long as system parameters are known.

- Theorem 1 indicates that for jamming, adaptive processing needs to adapt only to the jamming bearing, but not the magnitude of the jamming. The ICM is approximately invariant as long as the steering matrix of jamming is unchanged. Therefore, jamming filters can also be pre-built.

- Theorem 2 indicates that the effect of changes on the power of the radar (which normally incurs a variation in k_c), and/or the jammer power (which normally incurs a variation in k_j), and/or the thermal noise levels, on the optimum processor as given in Equation (20), is insignificant and can be ignored. Such variations only introduce an arbitrary scalar to the processor. As we know, this arbitrary scalar has no effect on the processor. This also suggests that in constructing PSTAP processor, there is no need to know the exact and absolute thermal noise level.

- The invariance of the ICM is robust and able to sustain elevation angle uncertainties induced by undulation of the terrain surface.

4.5 Interpretation

Figure 32 depicts clutter and jamming ridges in the Doppler-azimuth plane. To reject the interference of clutter and jamming, the optimum processor places deep notches in the same position of the clutter and jamming ridges as shown in Figure 7 (note that Figure 7 shows two notches for two jamming signals, whereas only one jamming signal is depicted in Figure 32). The position of the clutter ridge is solely determined by the parameters of radar system and platform, but not the clutter itself (limited to the first-order general clutter model). Although the clutter intensity profile may vary significantly corresponding to different clutter environments, the position of the clutter ridge remains unchanged if the parameters of radar and platform are kept unchanged. Because the clutter notch is normally deep enough, the same notch can be used to reject different clutter intensity

profiles. That is, the adaptive processing needs to adapt only to the radar and platform parameters.

Similarly, the position of jamming ridge is solely determined by the jammer bearing and has little to do with the intensity of the jamming signal. The same notch can be used to reject jamming signals with different intensities, as long as their bearing is the same.

4.6 Implementation

With the assurance of Theorems 1 and 2, the implementation of PSTAP can be separated into two stages: building jamming filters and optimum weighting vectors prior to the mission, and simply calling the appropriate jamming filters and optimum weighting vectors to process data snapshots during the mission.

4.6.1 Prior to the mission

- For jamming: pre-build a library of jamming filters corresponding to different bearings in conjunction with different radar and platform parameters.

- For clutter: pre-build a library of optimum weighting vectors corresponding to different combinations of radar and platform parameters, search angles and Doppler frequencies. If the PRF is linked to platform velocity in such a way that $\beta = 2v_a T_r / d$ remains constant, the total number of possible combinations can be significantly reduced.

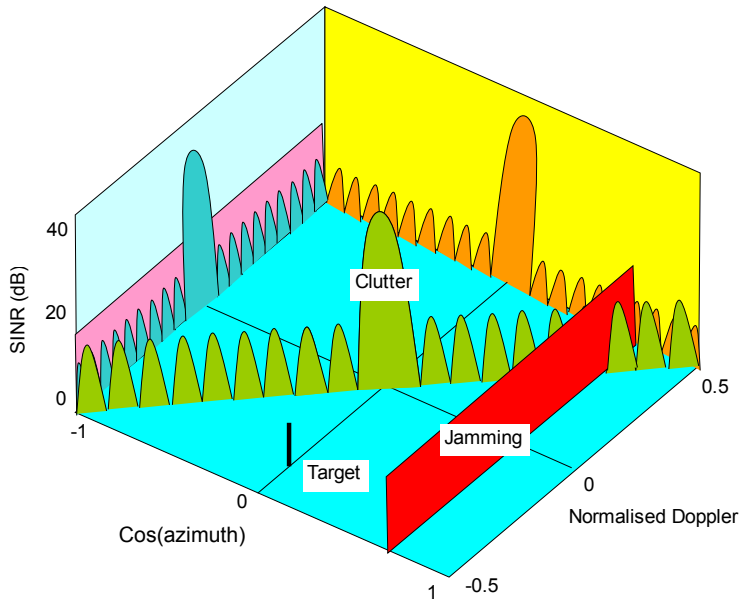

Figure 32: Clutter and jamming ridges in the Doppler-azimuth plane.

4.6.2 During the mission

- Determine the presence of jamming and its bearing, and call the appropriate jamming filters to filter the jamming interference. The rejection of jamming can also be achieved using beamforming techniques.

- Determine the radar and platform parameters and call the appropriate optimum weighting vectors to process the jamming-filtered snapshots to determine the presence of moving targets.

- If necessary, update the jamming filter library and optimum weighting vector library to compensate for changes in the radar and platform parameters.

5. Numerical Results

This Section presents some numerical results using both a generic airborne side-looking phased-array model and real airborne radar data collected by the MCARM system. Various issues including range ambiguity, clutter Doppler spectrum and platform motion which incur temporal and spatial decorrelation are discussed, and appropriate formulas are used to process the MCARM data for detecting desired signals which are many tens of dB below the clutter.

5.1 Results from a Generic Model

The generic model presented in Section 3, as well as clutter pattern cases 1, 2 and 3 presented in Section 4 were used for the simulation. The CMs $\mathbf{R}_{u(1)}$, $\mathbf{R}_{u(2)}$ and $\mathbf{R}_{u(3)}$ correspond to clutter pattern cases 1, 2, and 3, respectively. Jamming and thermal noise described in Section 3 remain unchanged for all calculations. To examine the performance of the PSTAP processor, its SINR is compared to that of the real-time STAP processor. In general, the SINR given previously in Equation (22) may be re-expressed as,

$$SINR = \frac{\sigma^2 \xi_t \left| \mathbf{w}_{opt(i)}^H \mathbf{v}_t \right|^2}{\mathbf{w}_{opt(i)}^H \mathbf{R}_{u(j)} \mathbf{w}_{opt(i)}} \tag{52}$$

If $i = j$ in Equation (52), the processor becomes the familiar real-time STAP, as the optimum weighting vector is calculated from the corresponding CM. If $i \neq j$ in Equation (52), the processor can be considered as PSTAP, because the optimum weighting vector $\mathbf{w}_{opt(i)}^H$ resulting from clutter case i is used to process data obtained from clutter case j.

Because the ICM correlation is the least when $\beta = 1.2$, as shown in Figure 22, we use this scenario to compare SINRs computed from real-time STAP and PSTAP. The results are

shown in Figure 33. It can be seen that all three fully adaptive curves are nearly identical, so are all three partially adaptive curves, irrespective of whether it is STAP ($i = j$) or PSTAP ($i \neq j$). For the partially adaptive, the algorithm of element-space, pre-Doppler with $K_t = 2$ (Ward, 1994) was used in the simulation.

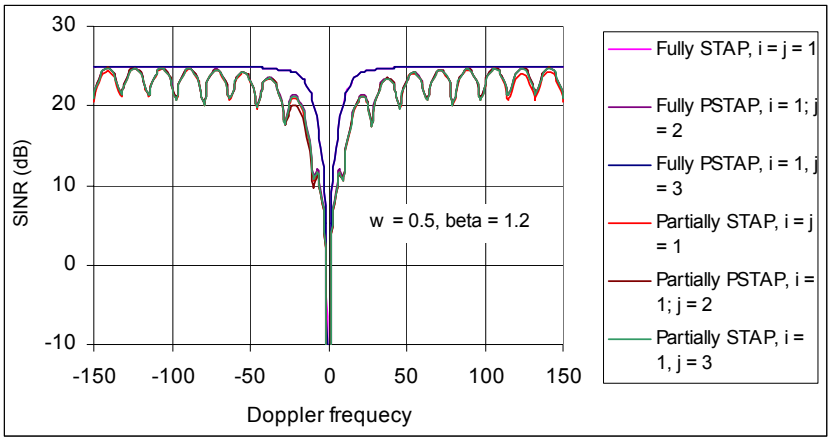

Figure 33: Comparison of SINR for STAP ($i = j$) and PSTAP ($i \neq j$). It seems that there are only two curves instead of six shown, because the three fully adaptive SINRs are nearly identical, so are the three partially adaptive SINRs.

Snapshots of clutter, jamming, noise and target are generated, in which the real part and imaginary part of clutter, jamming and noise are random and obey the $(0,1)$ Gaussian distribution, and the target signal has a constant Doppler and a constant magnitude. These snapshots are shown in Figure 34. The SNR of target and noise is 0dB, clutter is 47dB above the noise, and two equal jamming signals are 38dB above the noise. Various processors were applied to these snapshots of individual signals as well as the sum of the signals. The results are given in Table 3 and Table 4 corresponding to the fully adaptive and partially adaptive processors, respectively. It can be seen from the tables, the SINR of the sum of the signals may vary and be about 2 dB lower than the optimum value, which might be due to the fact that simulated interference signals are not perfectly Gaussian (this can be confirmed that the SINR of χ_c is not very low). But an important point we want to make is that the performance of STAP and PSTAP processor are about the same.

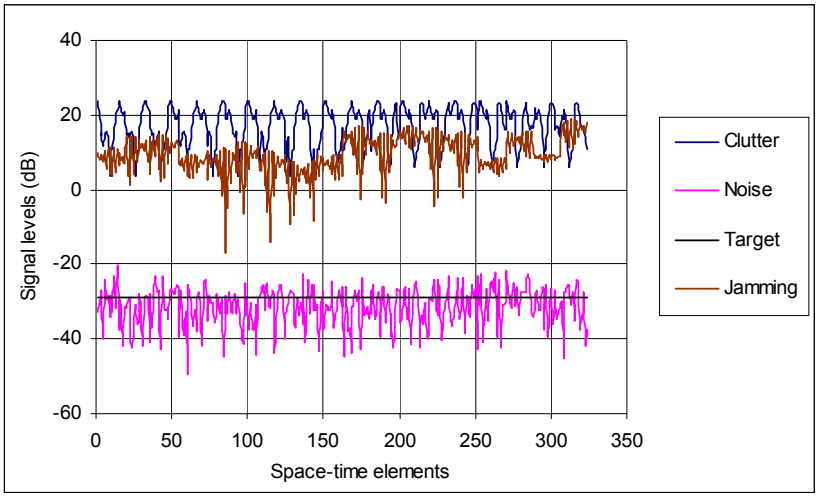

Figure 34: Snapshots of clutter, jamming, thermal noise and target signals.

Table 3: SINR values for various signals calculated using the fully adaptive STAP processors (R/T: real time STAP; P/B: pre-built PSTAP).

Clutter pattern	Processor	*SINR* (dB)				
		$\chi_t+\chi_c+\chi_j+\chi_n$	χ_t	χ_c	χ_j	χ_n
Case 1	R/T $(\mathbf{w}_{opt(1)},\mathbf{R}_{u(1)})$	22.5	25.0	14.9	-67.8	4.0
Case 2	R/T $(\mathbf{w}_{opt(2)},\mathbf{R}_{u(2)})$	25.3	25.0	-2.8	-63.3	3.8
	P/B $(\mathbf{w}_{opt(1)},\mathbf{R}_{u(2)})$	22.4	24.9	14.8	-67.9	4.0
Case 3	R/T $(\mathbf{w}_{opt(3)},\mathbf{R}_{u(3)})$	23.5	25.0	16.5	-66.8	3.9
	P/B $(\mathbf{w}_{opt(1)},\mathbf{R}_{u(3)})$	22.4	25.0	14.9	-67.8	3.9
	P/B $(\mathbf{w}_{opt(2)},\mathbf{R}_{u(3)})$	25.3	25.0	-2.8	-63.3	3.8

Table 4: SINR values for various signals calculated using partially adaptive processors (element-space, pre-Doppler $K = 2$, R/T: real time STAP; P/B: pre-built PSTAP).

Clutter pattern	Processor	*SINR* (dB)				
		$\chi_t + \chi_c + \chi_j + \chi_n$	χ_t	χ_c	χ_j	χ_n
Case 1	R/T $(\mathbf{w}_{opt(1)}, \mathbf{R}_{u(1)})$	24.5	22.8	10.9	-79.6	1.2
Case 2	R/T $(\mathbf{w}_{opt(2)}, \mathbf{R}_{u(2)})$	22.6	22.7	9.5	-44.8	0.9
	P/B $(\mathbf{w}_{opt(1)}, \mathbf{R}_{u(2)})$	23.9	22.1	10.3	-80.2	0.6
Case 3	R/T $(\mathbf{w}_{opt(3)}, \mathbf{R}_{u(3)})$	24.4	22.7	10.8	-79.7	1.1
	P/B $(\mathbf{w}_{opt(1)}, \mathbf{R}_{u(3)})$	24.4	22.7	10.8	-79.7	1.1
	P/B $(\mathbf{w}_{opt(2)}, \mathbf{R}_{u(3)})$	22.5	22.7	9.5	-44.9	0.9

5.2 Results from MCARM Data

Detailed descriptions of the multi-channel airborne radar measurement (MCARM) system can be found elsewhere (Sloper etc, 1996, Fenner, 1996). Some of the MCARM data analyses are also available (MITRE, 1999, RAFDCI, 1999, Sarker et al, 2001). A brief summary of the MCARM system is given in Appendix A.

This subsection focuses on the performance comparison between the real-time STAP and PSTAP processors. In doing so, some issues not considered in the previous sections, including range ambiguity, clutter Doppler spread and platform motion which incur temporal and spatial decorrelation, are discussed, and their effects are taken into account in order to construct a proper PSTAP processor.

The data cube #5-575 of Flight 5 was used for the analysis. The radar and platform parameters of #5-575 are given in Table 5 and Table 6, respectively.

Table 5: MCARM radar parameters

Frequency/ polarisation	PRF	CPI	Pulse width	Duty	Range resolution	PRI (us/gates)
1240 MHz/VV	1984	128	50.4 us	10%	0.8us	504/630

Table 6: MCARM platform parameters

Height	Velocity	Illumination	Crab angle	Antenna tilt angle from horizontal[5]
3488 m	100.1 m/s	Side-looking	7.28^o	5.11^o

[5]This angle is the sum of the antenna tilt angle relative to the platform plus the recorded platform roll angle.

5.2.1 Forming the Covariance Matrix Using the SMI Method

The SMI method uses sampled snapshots to compute the CM by (Ward and Kogon, 2004),

$$\hat{\mathbf{R}}_u = \frac{1}{K}\sum_{k=1}^{K} \boldsymbol{\chi}_k \boldsymbol{\chi}_k^H \tag{53}$$

The commonly accepted number of snapshot samples for forming the CM using the SMI method for the STAP analysis is $2MN$ (Reed et al, 1974, Ward 1994 Ward and Kogon, 2004). As described in Appendix A, for the Flight 5 medium PRF MCARM data, the number of receiver elements is $N = 22$, the number of pulses in a CPI is $M = 128.$ Therefore, approximately, a total of $2MN = 5632$ snapshots would be required to form the CM for STAP analysis. For the given data cube of #5-575, the total range bins are only 630. Besides, the first 200 bins or so have to be excluded, due to either the range less than the height (so the data do not reflect true clutter) or a leakage in range bin 68 (refer to the signal range profile shown in Figure A6). The usable range bins therefore, are far less that the theoretically required number.

To reduce the dimensionality, we only used one row of the receive modules ($N = 11$) , and 50 pulses ($M = 50$) in this report.

The CM of the so-called diagonally loaded SMI method is given by (Carlson, 1988, Ward and Kogon, 2004),

$$\hat{\mathbf{R}}_u = \frac{1}{K}\sum_{k=1}^{K} \boldsymbol{\chi}_k \boldsymbol{\chi}_k^H + \delta \mathbf{I} \tag{54}$$

where δ is a small value of the order of the system thermal noise level.

The diagonally loaded SMI method consistently outperforms the classical SMI method (Carlson 1988). It generally has a better adaptive sidelobe pattern, is more robust to the mismatch, and needs fewer snapshots (Ward and Kogon, 2004). Mathematically, by adding a small positive value to all the diagonal elements, the diagonally loaded SMI method guarantees the CM to be positive definite and invertible. Our simulation has confirmed the above reports, and therefore only the results of the diagonally loaded SMI will be reported.

According to MITRE (1999), a moving target with a large radar cross-section (RCS), referred to as a Sabreline, having a Doppler of approximate 522 Hz should appear in range bin 320. Unfortunately, for unknown reasons, the target signal has not been convincingly detected from the recorded data (MITRE, 1999, Sarkar, et al, 2001). For range bin 320 as the range bin of interest, initially we selected the sample range bins from 200 to 600 with the exclusion of range bins of interest itself and its 5 near and 5 far range bins to compute the CM. That is,

$$\hat{\mathbf{R}}_{u(k)} = \frac{1}{(600-200+1-11)}\left[\sum_{i=200}^{600}\boldsymbol{\chi}_i\,\boldsymbol{\chi}_i^H - \sum_{i=k-5}^{k+5}\boldsymbol{\chi}_i\,\boldsymbol{\chi}_i^H\right] + \delta\,\mathbf{I} \qquad (55)$$

where k is the range bin of interest, and δ used in the simulation was 70dB below the mean clutter.

It can be seen from Equation (55) that a total about 400 snapshots were used for computing the CM with a dimension of $11\times 50 = 550$. The number of samples seems to be still less than the required $2MN = 1100$. In fact the sample requirement of twofold the dimension of the CM can be relaxed. Because the CM of the MCARM data is assumed to have a structure of $\mathbf{R}_u = \mathbf{R}_c + \sigma^2\mathbf{I}$, the diagonally loaded SMI method usually only requires a minimum of $2r_c$ iid samples to form a reliable CM, where r_c is the rank of $\mathbf{R}_c$, and normally $2r_c << 2MN$ (Steiner and Gerlach, 1998 and 2000, Gerlach and Picciolo, 2003, Bresler, 1988). The number of sample snapshots in Equation (55) is 390, much greater than $2r_c$. Indeed, we found that a further increase/decrease in the number of sample snapshots makes little difference in the CM and the ICM. In fact more samples are available. Because only the data of the first 50 pulses are used, the data of the next 50 pulses could provide another set of iid samples. Furthermore, the data collected by the second row of the antenna can also be considered as another set of iid samples, since the second row of the antenna is identical to the first row of the antenna. Because the complex conjugate operation is involved in the computation, the phase difference between the first and the second rows due to their positions relative to clutter is not of concern in calculating the CM.

The SINR of STAP calculated from the CM obtained by Equation (55) is shown in Figure 35. Initially we thought that the small notch with the Doppler frequency about 300 Hz next to the clutter notch (note that the clutter Doppler frequency is not zero due to the crab angle) might be due to unknown interferences such as the interference of the platform to the radar. Careful examination using PSTAP (because PSTAP does not require any sample data) later indicated that it is due to a target signal in the range bin 299. With the exclusion of target range bin 299 and its 10 near and 10 far neighbouring bins, the CM is re-calculated and the resultant SINR of STAP is also shown in Figure 35. The disappearance of the small notch can be viewed. This also indicates one of the potential problems of STAP using the SMI method. If target range bins are included in the sample data without awareness, STAP will treat the target signal as an undesired signal, the performance of the processor then degrades.

The choice of δ in (55) for the diagonally loaded SMI method may be justified by examining the eigenvalues of the CM. The value of δ should be smaller than those significant eigenvalues of the CM. The eigenvalues of the CM without diagonally loading are shown in Figure 36 together with the comparison of the eigenvalues of the CM with diagonally loading $\delta\mathbf{I}$, where δ was 70dB below the mean value of the diagonal elements of the CM. It can be seen that adding $\delta\mathbf{I}$ only affects the eigenvalues ranked beyond 300 or so. Theoretically the rank of $\mathbf{R}_c$ should be much less than 300, according to Brenna's Rule given in (9). We also tried different values of δ, the results are not sensitive to δ in the range of 60-80dB below the mean value of the diagonal elements of the CM. Further

decease in δ did not seem to improve the results as in that case the numerical error would become dominant.

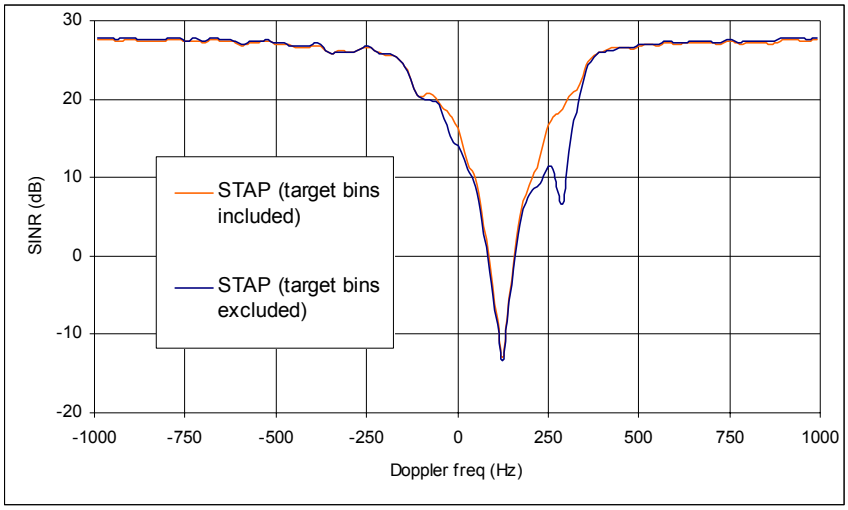

Figure 35: STAP SINR comparison using the diagonally loaded SMI method. If target bins are included in the sample data without awareness, the performance of the processor might degrade.

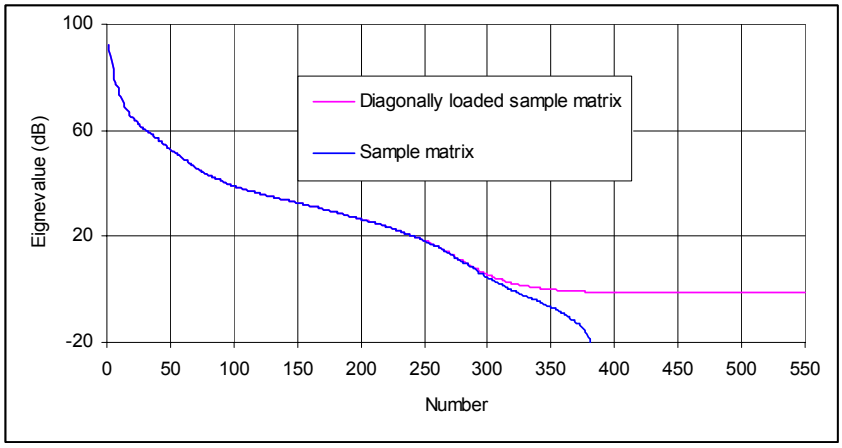

Figure 36: Eigenvalues of the sample covariance matrix compare to eigenvalues of the diagonally loaded covariance matrix.

5.2.2 Crab Angle Correction

A comparison between the preliminary SINR computed from the simulated CM presented in Section 2 and the SINR computed from the measured CM is shown in Figure 37. Because various gains and losses in process stages are unknown, the value of the measured SINR is adjusted and matched to the theoretical value of the simulated SINR.

Due to the crab angle, the Doppler frequency for the centre of the notch drifts from 0 Hz even though the antenna was looking at broadside. It can be noted that the centre of the notch for the simulated SINR does not point to the same Doppler frequency as the measured SINR does. This may be explained as the measurement error in the crab angle, as it is difficult to measure accurately. In the simulation a further 1^{o} was added to the recorded crab angle of 7.28^{o}, so the centre of the notch points to the same Doppler frequency as the measured SINR, as shown in Figure 37. It should be pointed out, however, that the effect of such a small adjustment in the crab angle on the performance of the PSTAP would be little. The point here is to demonstrate that the accurate system parameters but no single real-time sample data are required in forming the PSTAP weighting vectors. On the other hand, ample real-time sample data but not system parameters are required in forming the STAP weighting vectors.

The notch of the preliminarily simulated SINR is much narrower than that of the measured SINR. It can be expected that if such a preliminarily simulated SINR is used to process the measured data, the clutter would not be sufficiently suppressed. Therefore the effects of temporal and spatial decorrelation due to range ambiguity, clutter Doppler spread and platform motion has to be taken into account to modify the simulated SINR. The following subsection addresses this issue.

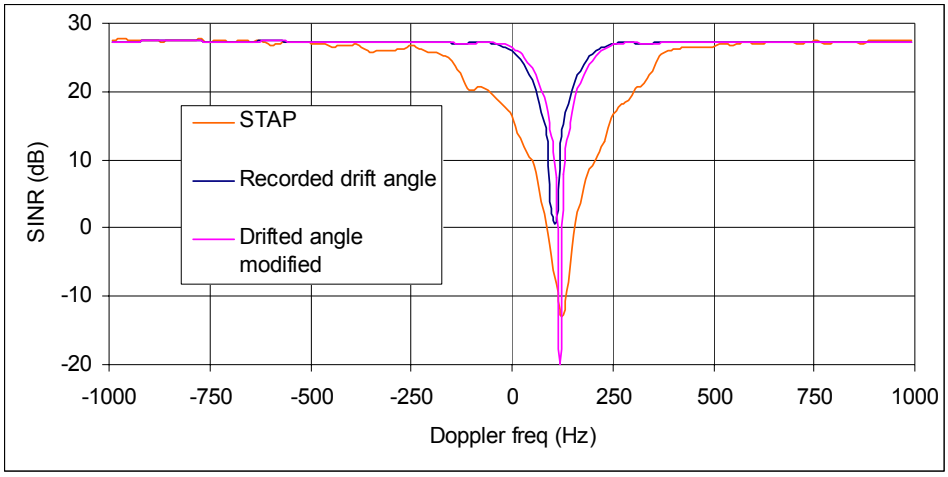

Figure 37: Comparison of the preliminarily constructed PSTAP SINR to the STAP SINR.

5.2.3 Temporal and Spatial Decorrelation Effects

Klemm (2002) lists four contributions to the decorrelation. They are,

1. Range walk (platform motion, temporal correlation);
2. System bandwidth (ambiguity function $\chi(\tau,0)$ for antenna elements, spatial correlation);

3. Clutter intrinsic motion (clutter temporal correlation);
4. Doppler spread in range (temporal and spatial correlation, only if the Doppler is range dependent).

Klemm (2002) has reported detailed simulations of the above four decorrelation effects. According to Klemm (2002),

- The effect of range walk is insignificant for radars with coarse range resolution (e.g., >100 m, the range resolution of MCARM data is 150m).
- The effect of system bandwidth is insignificant if the length of the antenna is small. The effect may become significant for synthetic aperture radar (SAR) data.
- There is no Doppler spread in range for the side-looking scenario, so the last term is also insignificant.

Therefore, among the four correlation models, we only need to consider the effect due to clutter intrinsic motion.

However, for medium PRF radar, range ambiguity is unavoidable. The steering angle of ambiguous range is different from the steering angle of the true range. The effect of clutter contribution due to range foldover can be considered as an effect of decorrelation, since the effect of range foldover also widens the clutter notch.

Effect of range ambiguity

For a medium PRF, the range ambiguity is unavoidable. Clutter returns from different ranges have different steering matrices. Assuming that the clutter returns from different patches are uncorrelated, the CM for the multiple range case is,

$$\mathbf{R}_c = \sum_{k=1}^{r} \mathbf{V}_k \mathbf{\Sigma}_{kc} \mathbf{V}_k^H \tag{56}$$

where r is the number of multiple ranges. For instance, for range bin 320 of MCARM data #5-575, the true range is 38.4 km, and the 1st and 2nd ambiguous ranges are 114 km and 189.6 km, respectively. Assuming clutter against grazing angle obeys the $\sin\theta$ function, where θ is the grazing angle, and the clutter power decays as $1/R^3$ as specified in radar Equation (7) (the cutter patch area A is proportional to R), the clutter profiles for the above three different ranges are obtained as shown in Figure 38.

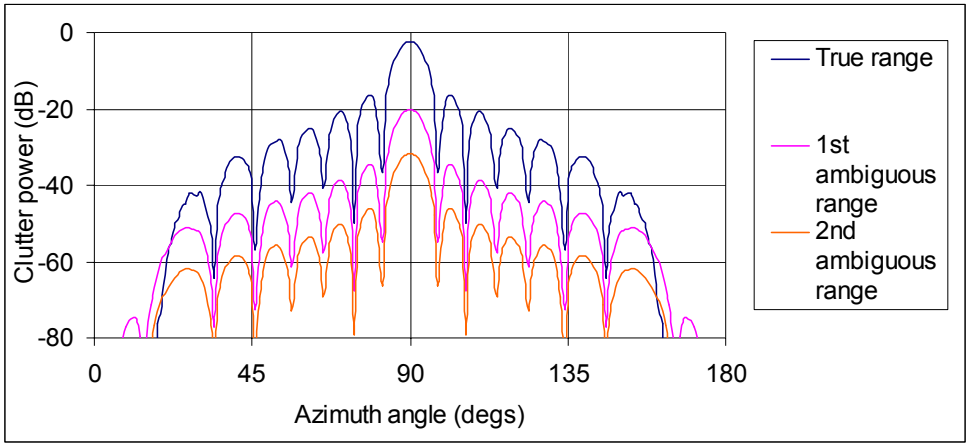

Figure 38: Clutter profiles corresponding to the true range, 1st and 2nd ambiguous ranges (only the frontlobe part is shown).

The SINR with the range ambiguity being taken into account is shown in Figure 39. It can be seen that the notch has been widened, but is still not as wide as obtained from the STAP.

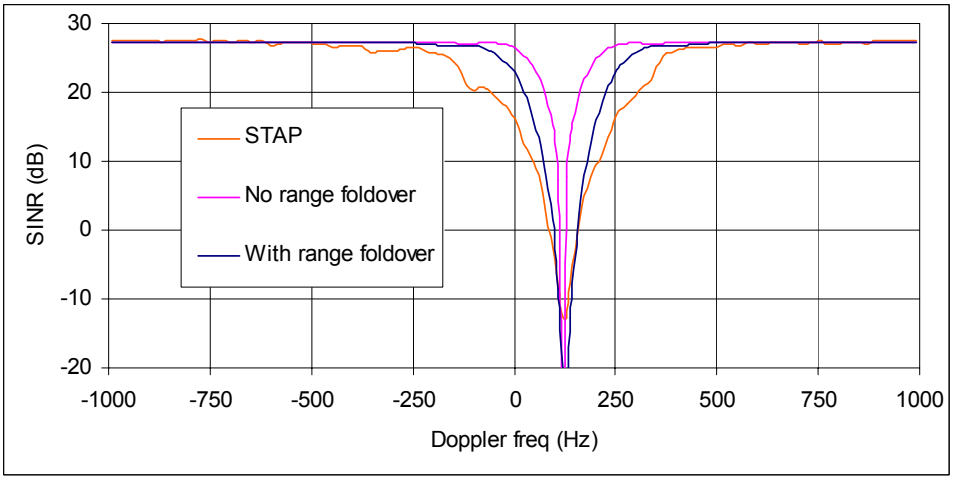

Figure 39: Constructed PSTAP SINR with the range ambiguity being taken into account in comparison with the STAP SINR.

Due to range foldover, theoretically, data collected from the first pulse, which do not contain components of multiple range clutter, should be statistically different from the data collected from the following pulses. This difference is not of concern to STAP if the SMI method is used, as the difference is also sampled. For PSTAP, this might be an issue

unless the model takes the difference into account. Because the model assumes that data collected by all pulses are statistically the same, in the process the data collected by the first pulse were excluded, and the actual data used were the data collected by the 2nd to 51st pulses for PSTAP. For the comparison purpose, the same data were used for STAP, although there is no need to exclude the data of the first pulse for STAP.

Next we also include the effect of clutter intrinsic motion.

Clutter intrinsic motion

Under windy conditions surface clutter echoes fluctuate due to the motion of moving parts of scatterers. The Doppler spectrum of land clutter is exponentially distributed and there is a large dc component in the spectrum (Billingsley, 2002), from which the correlation can be derived. Such a correlation is then generally non-Gaussian. Other researchers argue that a radar system performs linear averaging at many stages including antenna, IF bandpass filters, baseband anti-aliasing filters, pulse compression filters etc, so that the central limit theorem applies in general (Goldstein and Guerci, 2004). The resultant correlation is Gaussian. Figure 40 shows the measured temporal correlation at L-band due to clutter intrinsic motion under different wind conditions (Billingsley, 2002). It can be seen that these correlations are close to Gaussian distributions.

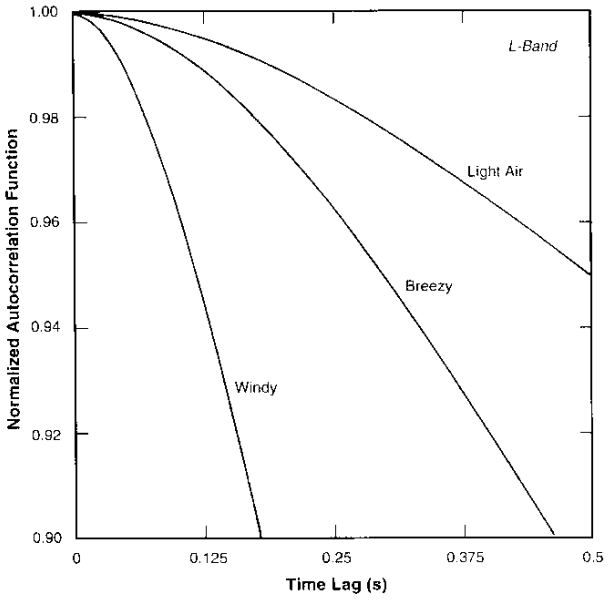

Figure 40: Measured temporal correlation at L-band due to clutter intrinsic motion (Billingsley, 2002).

The Gaussian distributed correlation model due to clutter intrinsic motion is given by (Klemm, 2001),

$$\rho_{mp}^{(c)} = \exp\left[-\frac{B_c^2(m-p)^2}{8}\right] \tag{62}$$

where $B_c = B / f_{PRF}$ is the normalised clutter bandwidth, and B is the clutter bandwidth.

According to Long (2004), the Doppler velocity of land clutter with a 60dB spectrum (signal decays 60dB from the centre frequency of 0 Hz) is often $<1 m/s$, giving,

$$B \le 2\frac{2v}{\lambda} = 2\frac{2\times 1}{0.24} = 16.7\,Hz \tag{63}$$

Another way of calculating the clutter bandwidth is (Ward, 1994),

$$B = \frac{8\pi\sigma_v}{\lambda} \tag{64}$$

where σ_v is the standard deviation of clutter velocity, whose value typically varies from 0 to 0.5m/s for land clutter (Nathanson, 1999). If we select $\sigma_v = 0.5 m/s$, we have,

$$B = \frac{8\pi\times 0.5}{0.24} = 52\,Hz \tag{65}$$

In the construction of the PSTAP processor, the bandwidth given in Equation (65) was used, because it seems that the calculated SINR of PSTAP is closer to the SINR of STAP for the MCARM data. The SINR comparison among the SINR of STAP and the SINR with range foldover only, and the SINR with multiple range as well as clutter Doppler spread of PSTAP is shown in Figure 41. It can be seen that the SINR of PSTAP, after the effects of range foldover and clutter Doppler spread are taken into account, is very close to the SINR of STAP. The result of PSTAP therefore can be expected to be approximately the same as the result of STAP. The PSTAP SINR has a deeper notch than STAP SINR indicating the PSTAP has a greater capability to suppress clutter than required, which is however not our concern. STAP (PSTAP) is not designed for detecting targets whose Doppler is in the region of clutter Doppler.

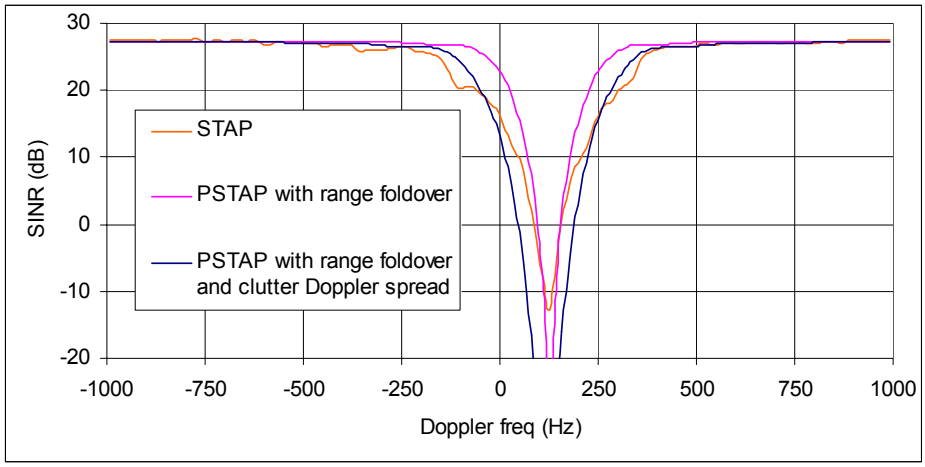

Figure 41: SINR comparison among the STAP SINR and the PSTAP SINR with range foldover only and the PSTAP SINR with range foldover as well as clutter intrinsic motion.

5.2.4 Results

Nobody was able to find the supposed target, Sabreline in range bin 320 or elsewhere with an approximate Doppler frequency of 522 Hz (MITRE, 1999, Sarkar, et al, 2001). Our process shows that although there is no target in range bin 320, a target with a Doppler frequency about 300 Hz, indeed has been found in range bin 299. If this target is the Sabreline, what causes the range bin and frequency shift is unknown, possibly due to experimental measurement errors. This data set has been studied in many cases, but as far as we are aware, this is the first time that a target has been declared found in the data set. The spectrum of clutter plus target signals in range bin 299 is shown in Figure 42. It can be seen that the target cannot be identified without clutter suppression. The results of clutter being suppressed using PSTAP and STAP are shown in Figure 43. Comparing the results of PSTAP and STAP, we can seen that the sidelobe level of PSTAP much more regular and lower than that of STAP. This might be attributed to the fact that the CM of PSTAP approaches ideal while the CM of STAP is only obtained from limited and inhomogeneous sample data.

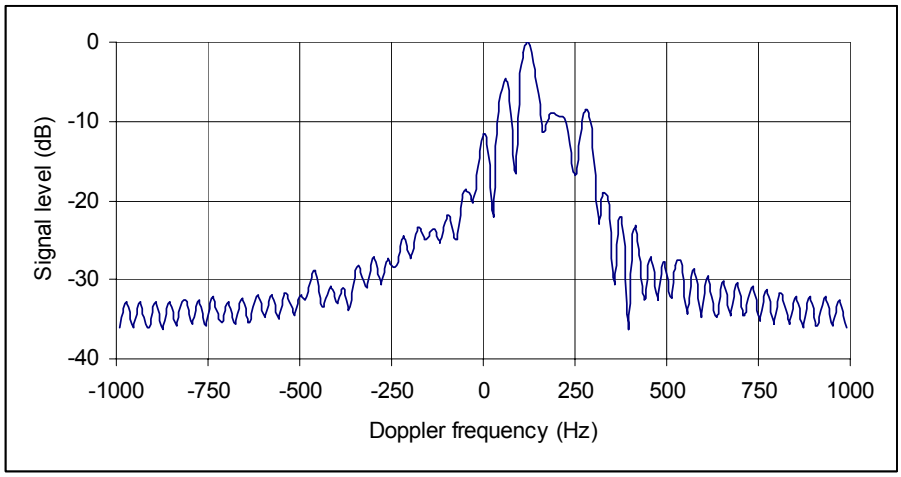

Figure 42: Spectrum of clutter plus target signals in range bin 299.

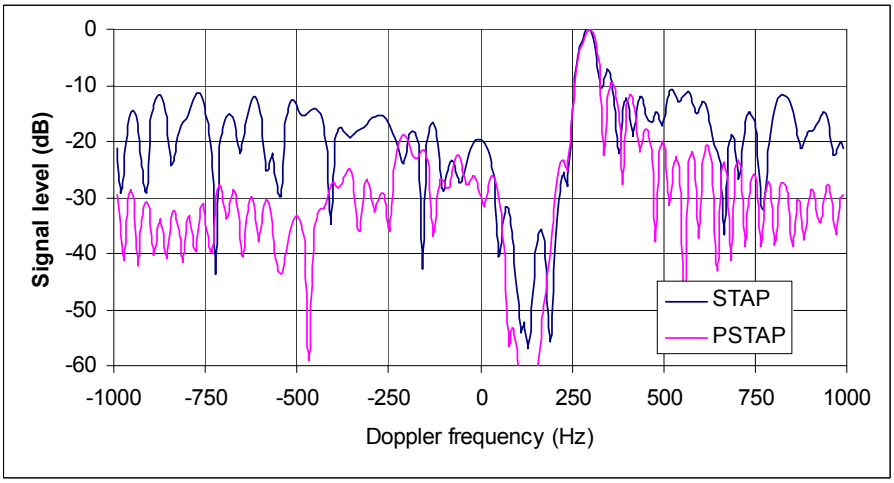

Figure 43: A target with Doppler frequency of 300 Hz in range bin 299 has been detected using both STAP and PSTAP processors.

Because each range bin corresponds to a specific elevation angle, so each range bin should have a corresponding set of weighting vectors of PSTAP. However, we have shown that the ICM is insensitive to a certain variation of the elevation angle (the penalty is only about 0.5dB). Therefore the same set of weighting vectors of PSTAP can be used to process different range bins. Figure 44 shows the result of PSTAP, where only one single set of

weighting vectors, corresponding to the middle range bin, was used to process all range bins 200-600. The target in the range bin 299 is obvious.

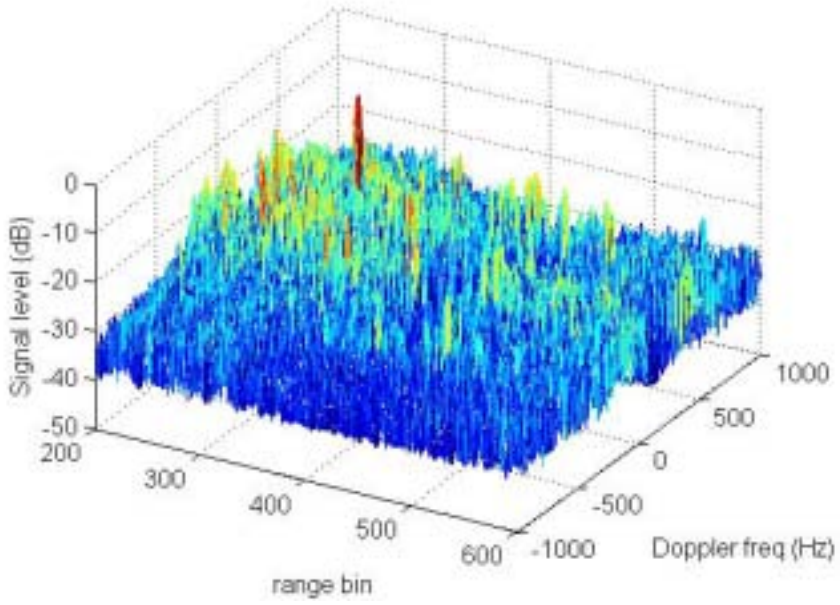

Figure 44: A target is detected using PSTAP. The same set of weighting vectors was used for all range bins.

In order to further assess the performance of PSTAP, range bins 320 and 350 were selected as range bins of interest. Because no target presents in these range bins, two artificial target signals, each with constant amplitude and constant Doppler frequency (Swirling 0 model), were injected into the original signal. In particular, the amplitudes of the two injected signals are the same with levels at 40 and 30dB below the mean clutter, respectively, for each test case. Their Doppler frequencies are –300 Hz and +600 Hz, respectively. The mean clutter amplitude of a snapshot is defined as,

$$E\{\| \boldsymbol{\chi} \|^2\} = \frac{1}{MN} \sum_{i=1}^{MN} |\chi_i| \qquad (68)$$

The amplitude of the clutter snapshot in range bin 320 is shown Figure 45. Shown in the figure is also the injected target signal with a constant Doppler frequency and a constant amplitude but 40dB below the mean clutter. The Doppler spectrum of clutter in range bin 320 is shown in Figure 46.

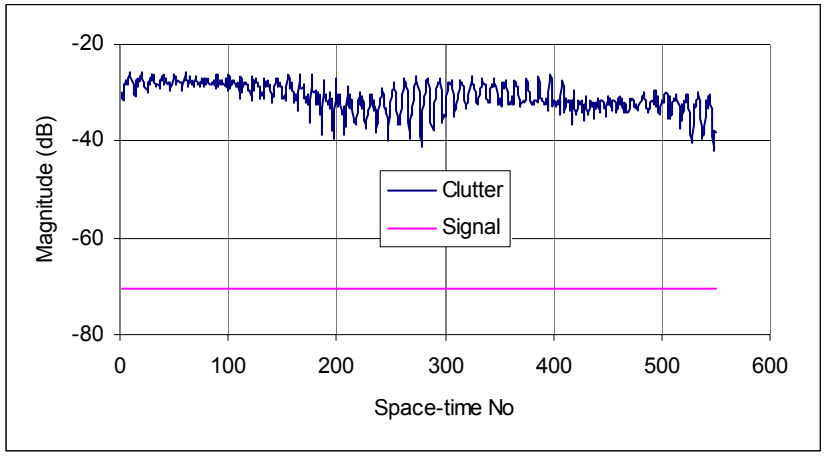

Figure 45: Snapshots of clutter in range bin 320 and the injected target signal which is 40dB below the clutter.

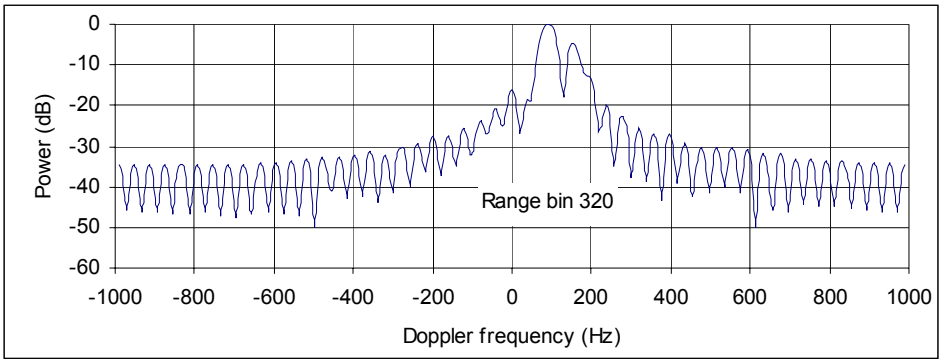

Figure 46: Doppler spectrum of clutter in range bin 320. The Doppler spread of the mainlobe clutter is about 200 Hz.

The performance of two processors, ie, diagonally loaded SMI STAP and PSTAP, are compared. The results are shown in Figure 47 to Figure 48. Observing these plots we can conclude that the performance of the PSTAP is about the same as that of the diagonally loaded SMI STAP. The sidelobes of PSTAP near the notch are a few decibels higher than that of STAP especially when the target signal is weak, which can be easily overcome if necessary. In fact if we re-examine the STAP SINR and PSTAP SINR in Figure 41, we can see that the PSTAP SINR is a few decibels higher than that of the STAP SINR in that

Doppler region. This may be due to some decorrelation effect which has not been considered and included. If the PSTAP SINR is further modified, these high sidelobes would be suppressed. This issue will be further investigated in the future.

In order to further examine the performance of the PSTAP for the whole Doppler frequency spectrum, targets with low and high frequencies were injected into the original signal, and the results compared. Figure 49 shows the processor comparison for detecting two injected low frequency (-50 Hz and +300 Hz) and low magnitude (30dB below clutter) target signals, while the processor comparison for detecting two injected low frequency (–100 Hz and +350 Hz) and low magnitude (30dB below clutter) target signals is shown in Figure 50. Finally compares the processors for detecting two injected high frequency (–900 Hz and +900 Hz) and low magnitude (40dB and 30dB below clutter) target signals. These comparisons again indicate that the performance of the PSTAP is about the same as that of the diagonally loaded SMI STAP.

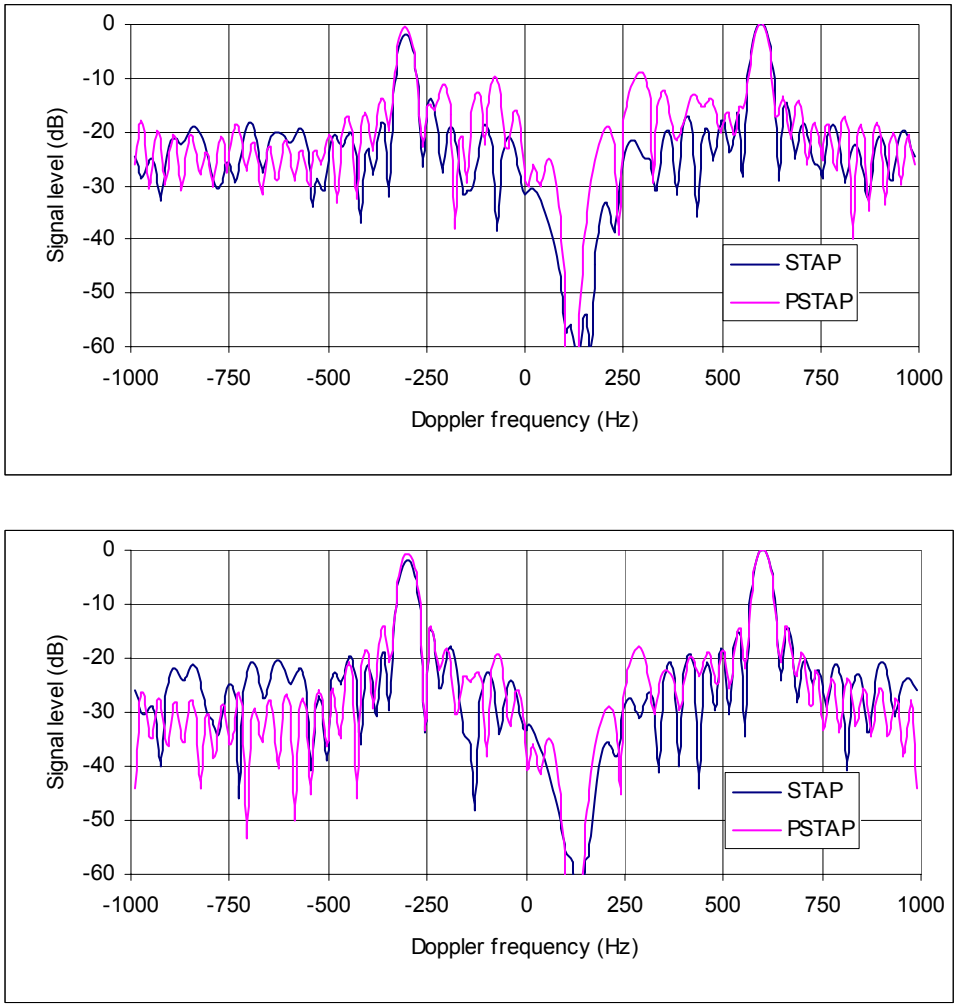

Figure 47: Processor comparison for detecting targets 40dB (top) and 30dB (bottom) below the clutter at –300 Hz and +600 Hz in range bin 320.

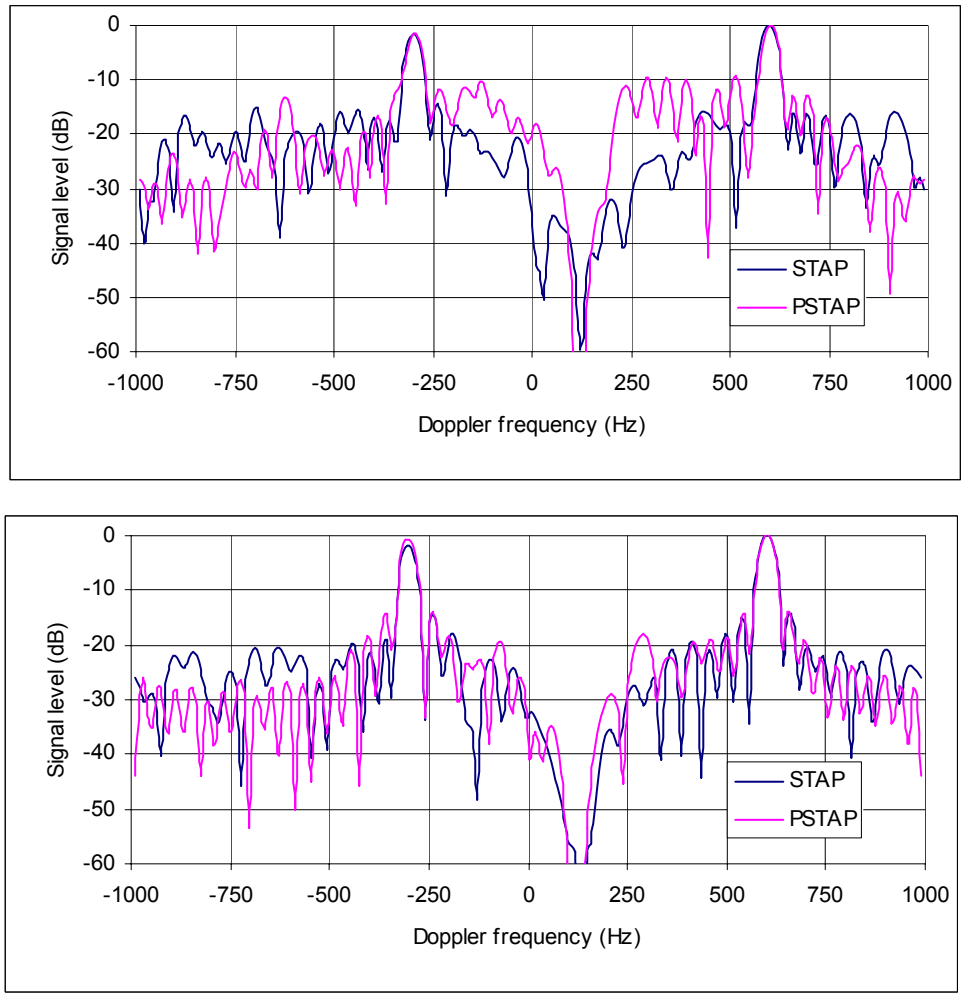

Figure 48: Processor comparison for detecting targets 40dB (top) and 30dB (bottom) below the clutter at –300 Hz and +600 Hz in range bin 350.

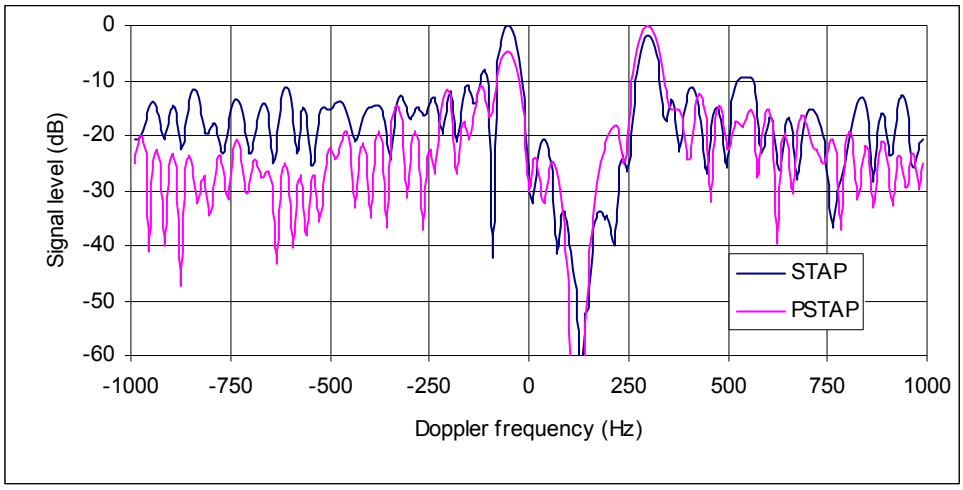

Figure 49: Processor comparison for detecting targets 30dB below the clutter at –50 Hz and +300 Hz in range bin 320.

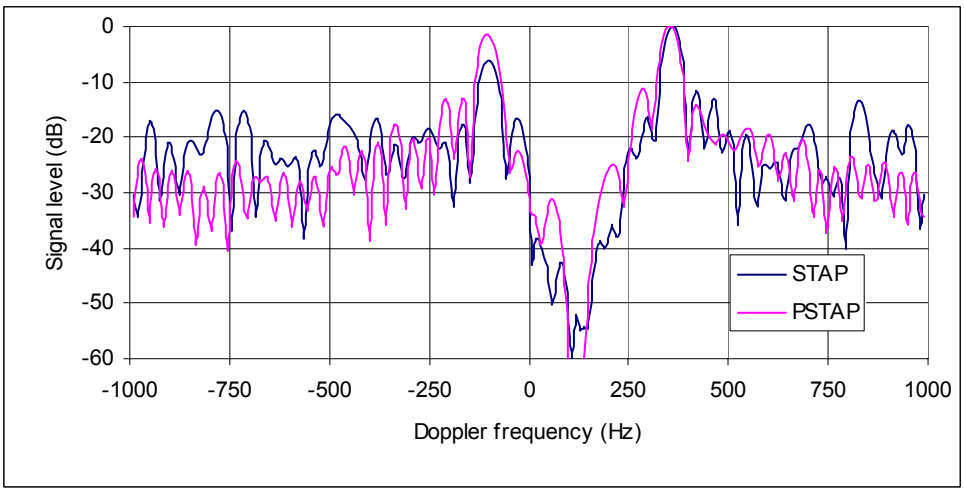

Figure 50: Processor comparison for detecting targets 30dB below the clutter at –100 Hz and +350 Hz in range bin 320.

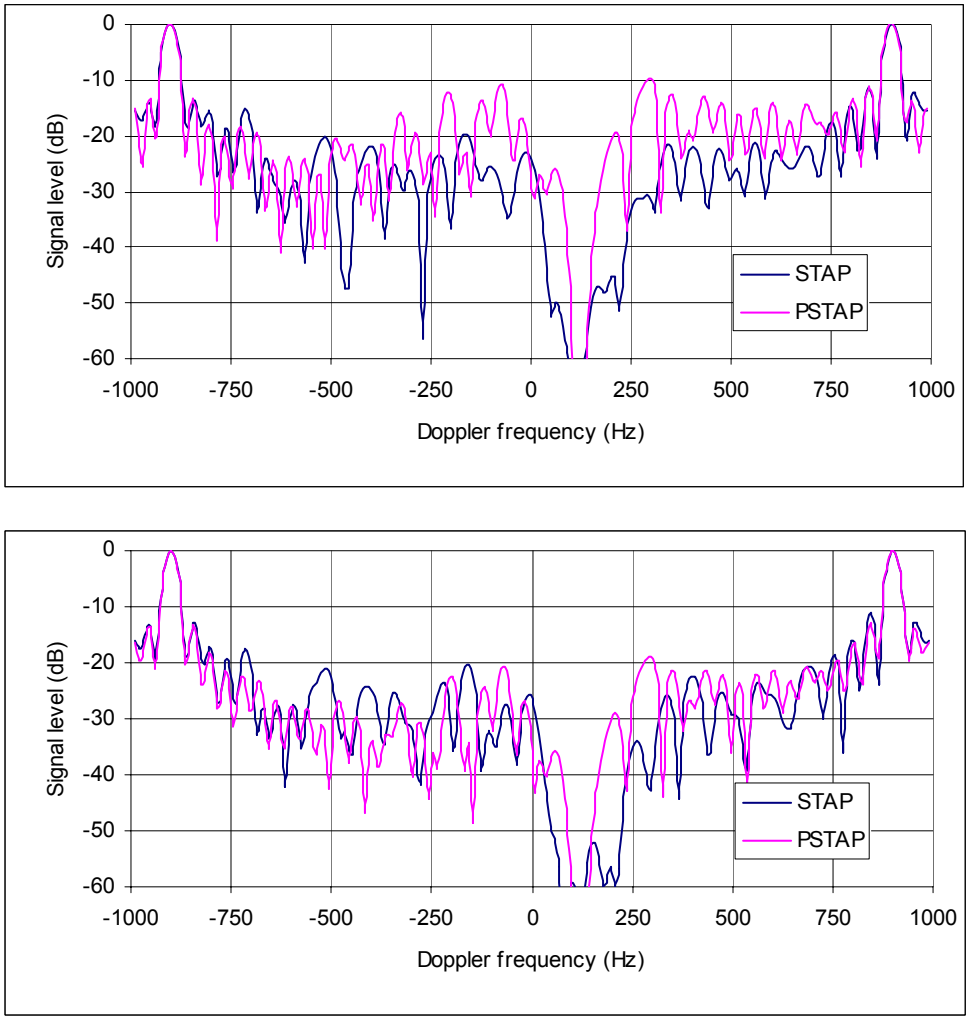

Figure 51: Processor comparison for detecting targets 40dB (top) and 30dB (bottom) below the clutter at –900 Hz and +900 Hz in range bin 320.

6. Conclusions

With phased-array radar technologies, STAP is optimal in terms of detecting moving target signals embedded in much stronger interference signals such as surface clutter. Implementation of real-time STAP algorithms is however not practical due to the time taken to compute the covariance matrix and its inverse. Partially adaptive (reduced dimensionality) STAP algorithms may significantly reduce the computation requirement, but the algorithms are based on a necessary condition that the structure of the covariance matrix is Toeplitz-block-Toeplitz. If the covariance matrix is not strictly Toeplitz-block-Toeplitz, which is almost always the case for the measured data, the expected processing gain of the partially adaptive STAP processors greatly degrades.

A significant contribution of this report is the indication of the inverse of the covariance matrix (ICM) to be approximately invariant to variations of clutter. Two Theorems have been proposed and their mathematical proofs provided. Various numerical examples have been given for confirmation of the Theorems. The following conclusions have been deduced:

- For clutter, STAP needs to adapt only to system parameters (both radar and platform). Variations in clutter intensity, which will result in significant variations in the elements of the covariance matrix, cause little variations in the elements of the inverse of the covariance matrix;

- For jamming, STAP needs to adapt only to the bearing of jamming. Variations in jamming intensity, which will result in significant variations in the elements of the covariance matrix, cause little variations in the elements of the inverse of the covariance matrix.

In consequence, a pre-built space-time non-adaptive processor (PSTAP) has been proposed. The PSTAP is not an adaptive processor in the broad meaning of adaptive processing as no adaptive processor can be pre-built. However, it does have a capability to cope with changes in clutter, due to the invariance of the inverse of the covariance matrix (the knowledge of the clutter environment is not really required). Therefore the performance of the PSTAP may approach that of the STAP as long as the system (radar and platform) parameters are known.

The idea of PSTAP is to construct a library of weighing vectors a priori, either by modelling or using flight data. Each weighting vector corresponds to a specific set of the radar and platform parameters. Using such a processor the computational bottleneck is completely removed. Theoretically, if the system parameters are known, the proposed PSTAP can achieve the same coherent processing gain as real-time STAP. In reality, due to the fact that the CM for real-time STAP is difficult to obtain accurately, PSTAP may even achieve better results if all the system parameters required for the construction of the processor are known precisely.

Before the mission, a library of optimum weighting vectors corresponding to various combinations of radar and platform parameters can be pre-built without knowledge of the actual clutter environment. A library of jamming filters can also be pre-built corresponding to various jamming bearings. During the mission, the collected data are first analysed to determine the existence of the jamming. Either appropriate jamming filters or beamforming techniques are applied if jamming is detected. The jamming-free data are then multiplied with appropriate weighting vectors from the library to generate the output. The pre-built libraries may need updating once the radar and platform parameters undergo changes.

If a real radar system is difficult to model (for instance, the array may not be rigorously linear and the effect of the platform on the antenna system may be difficult to model etc), the library may be pre-built based on data collected from previous missions. Because of

the nature of its invariance, the ICM from different clutter environments should be approximately the same. Therefore, the optimum weighting vectors obtained from previous missions can be directly used for future missions, irrespective of clutter environments, as long as the radar and platform parameters remain unchanged.

There are usually a large number of possible combinations of radar and platform parameters, and so a large number of weighting vectors have to be pre-built. If the radar PRF is linked to the platform velocity in such a way that $\beta = 2v_a T_r / d$ remains constant, the number of combinations can be significantly reduced. Also because the ICM is not very sensitive to the changes in steering angle varying from range bin to range bin, the same set of weighting vectors can be used to process different range bins, which has been demonstrated in the process of the MCARM data as shown in Figure 44.

A robust analysis for PSTAP has been carried out. Uncertainties incurred in the steering angles caused by possible undulating terrain surfaces as well as variations in clutter intensities have been studied. It has been shown that the SINR loss of PSTAP is normally only about 0.2-0.5dB even for the most extreme variations in the terrain surface.

Numerical examples have been presented. The first numerical example was for a generic airborne radar model. Cases of clutter coefficients randomly fluctuating up to $\pm 15dB$ (simulating an environment much worse than any inhomogeneous environment) were compared to the usual case of the constant clutter coefficient (simulating a homogenous clutter environment) showing that the resultant ICMs are almost identical. The correlation coefficient r^2 for all pairs of ICMs compared is higher than 0.99 showing that the ICM is insensitive to variations in the clutter environment. The PSTAP processor performs the same as the STAP processor for all scenarios simulated.

The second numerical example was to apply the PSTAP processor to MCARM data. In order to process the real data, some assumptions in the generic model have been modified. Temporal and spatial correlations due to both the radar system and clutter have been taken into account in order to built a realistic and appropriate PSTAP processor. It has been shown that the dominant decorrelation mechanisms include multiple range and clutter intrinsic motion. A target in the #5-575 data set has been convincingly detected using PSTAP. Finally the PSTAP processor has also been compared to the real-time STAP processor (the diagonally loaded SMI method) for detecting injected small target signals. It has been shown that the performances are about the same.

In conclusion, the PSTAP processor can be constructed purely from modelling, or alternatively based on date collected from previous missions.

7. Acknowledgement

The discussions with Drs D Madurasinghe, T Winchester, A Shaw and J Whitrow help to improve the readability of the report. Thanks are also due to Dr Madurasinghe for the indication of an error in the draft of the report. Finally Dr Whitrow helped correcting

grammar errors. Creative comments by the vetting officer, Dr J Fabrizio, are also acknowledged. The MCARM data was supplied by the Rome Laboratory, Air Force Material Command.

8. References

Billingsley, J B, *Low-Angle Land Clutter Measurements and Empirical Models*, William Andrew Publishing, New York, 2002.

Brennan, L E, and Staudaher, F M, "Subclutter visibility demonstration", Technical Report, RL-TR-92-21, Adaptive Sensors Incorporated, March 1992.

Bresler, Y, "Maximum likelihood estimation of a linearly structured covariance with application to antenna array processing", *Proceedings of the Fourth Annual ASSP Workshop on Spectrum Estimation and Modelling*, pp. 172-175, 3-5 Aug 1988.

Bodewig, E, *Matrix calculus*, 2nd edition, North-Holland Publishing, Amsterdam, 1959.

Carlson, B D, "Covariance matrix estimation errors and diagonal loading in adaptive arrays", *IEEE Trans on Aerospace and Electronic Systems*, vol. 24, no. 4, pp. 397-401, 1988.

Compton, Jr, R T, *Adaptive Antennas, Concepts and Performance*, Prentice Hall, New Jersey, 1988.

Dong, Y, "Models of land clutter vs grazing angle, spatial distribution and temporal distribution – L-band VV polarisation perspective", Research Report, DSTO-RR-0273, DSTO, 2004.

Fenner, D, and Hoover, W F, "Test results of a space-time adaptive processing system for airborne early warning radar", *Proceedings of IEEE 1996 National Radar Conference*, Ann Arbor, Michigan, 13-16 May 1996.

Gerlach, K, and Picciolo, M L, "Airborne/spacebased radar STAP using a structured covariance matrix", *IEEE Trans on Aerospace and Electronic Systems*, vol. 39, no. 1, pp. 269-281, January 2003

Goldstein, I C, Guerci, J R, "STAP II: Advanced techniques", tutorial slides, CD of the *Proceedings of 2004 IEEE Radar Conference*, Philadelphia Pennsylvania, 26-29 April 2004.

Klemm, R K, *Principles of Space-Time Adaptive Processing*, 2nd Edition, IEE, London, 2002.

Kreyenkamp, O, "Clutter covariance modelling for STAP in forward looking radar", *DGON International Radar Symposium 1998*, Munich, 15-17 Sept 1998.

Long, M W, "Radar clutter", Tutorial slides, CD of the *Proceedings of 2004 IEEE Radar Conference*, Philadelphia Pennsylvania, 26-29 April 2004.

Mardia, K V, Kent, J T, and Biddy, J M, *Multivariate Analysis*, Academic Press, London, 1979.

MITRE, "STAP processing monostatic and bistatic MCARM data", Final report prepared by MITRE, Centre for Air Force C2 Systems, Bedford, MA, 1999.

Nathanson, F E, Reilly, J P, and Cohen, M N, *Radar Design Principles*, 2nd Edition, Scitech Publishing Inc., 1999.

RAFDCI, "MCARM/STAP data analysis", Final report, Part I and II, prepared by Research Associates for Defence Conversion Inc., New York, 1999.

Reed, I S, Mallett, J D, and Brennan, L E, "Rapid convergence rate in adaptive arrays", *IEEE Trans on Aerospace and Electronic Systems*, vol. AES-10, no. 6, 1974.

Sarkar, T K, Wang, H, Park, S, Adve, R, Koh, J, Kim, K, Zhang, Y, Wicks, M C, and Brown, R D, "A deterministic least-squares approach to space-time adaptive processing", *IEEE Trans on Antennas and Propagation*, vol. 49, no. 1, January 2001.

Skolnik, M I, *Radar Handbook*, McGraw-Hill, New York, 1970.

Sloper, D, Fenner, D, Arntz, J, and Fogle, E, "Multi-channel airborne radar measurement (MCARM), MCARM flight test", Westinghouse Electronic Systems, final technical report, RL-TR-96-49, vol. 1, April, 1996.

Steiner, M, and Gerlach, K, "Fast converging maximum-likelihood interference cancellation," *Proceedings of IEEE 1998 National Radar Conference*, pp. 117-122, Dallas, TX, 12-13 May 1998.

Steiner, M, and Gerlach, K, "Fast converging adaptive processor for a structured covariance matrix", *IEEE Trans on Aerospace and Electronic Systems*, vol. 36, no. 4, pp. 1115-1126, Oct 2000.

Thomas, V, private communications, 2003.

Ward, J, "Space-time adaptive processing for airborne radar", Technical report TR-1015, Lincoln Laboratory, MIT, 1994.

Ward, J, and Kogon, S M, "Space-time adaptive processing (STAP) for AMTI and GMTI radar", tutorial slides, CD of the *Proceedings of 2004 IEEE Radar Conference*, Philadelphia Pennsylvania, 26-29 April 2004.

Wirth, W D, *Radar Techniques Using Array Antennas, IEE*, London, 2001.

Appendix A: MCARM System

Detailed descriptions of the Multi-channel airborne radar measurement (MCARM) system may be found in the relevant documents (Sloper, et al, 1996, Fenner, 1996). Some MCARM STAP data analyses are also available (MITRE, 1999, RAFDCI, 1999, Sarkar, et al, 2001,). This Appendix only provides a brief summary of the system.

The system is L-band, vertically polarised. The transmitter consists of 32 modules in two rows. Each module is formed by 4 antenna elements as depicted in Figure A1. Therefore, the transmitter pattern can be simulated by a phased array comprising 32-by-8 antenna elements. The azimuth spacing and elevation spacing are 4.3 and 5.54 inches, respectively. The azimuth tapering coefficients are close to uniform and their values from the centre are: 0dB, -0.0626dB, -0.1260dB, -0.1904dB, -0.2553dB, -0.3217dB, -0.3891dB and -0.4576dB (Thomas, 2003). A 20dB Taylor taper is used across the elevation elements. The actual tapering coefficients from the centre are: 0dB, -1.488dB, -4.662dB and –8.449dB (Sloper, et al, 1996). The simulated and the measured transmitter patterns (array as a whole) are shown in Figures A2-A3. It can be seen that the agreement between the simulated and measured patterns is reasonably good.

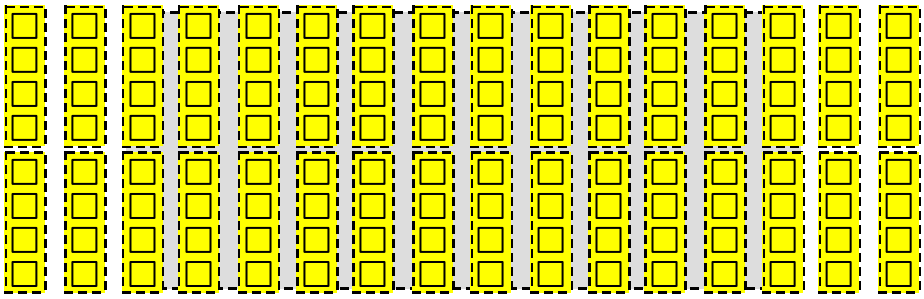

Figure A1: Structure of the antenna system: the transmitter consists of 32 modules while only the central 22 modules are used as the receiver elements.

The receiver (element) is modelled by a $\cos^{0.4}(\phi)$ function (frontlobe) which gives a 6dB beamwidth of 160^{o} for both the azimuth and elevation directions (Sloper, et al, 1996). A comparison between the simulated and measured module (4-by-1 elements) patterns is shown in Figures A4-A5. Similarly the agreement between the simulation and measurements is reasonably good. An exception is the azimuth pattern for the angle beyond the $\pm 60^{0}$ region. However, the steering angle is normally within $\pm 60^{0}$, so there is no need to modify the simulated receiver pattern to fit the measured pattern beyond the $\pm 60^{0}$ region.

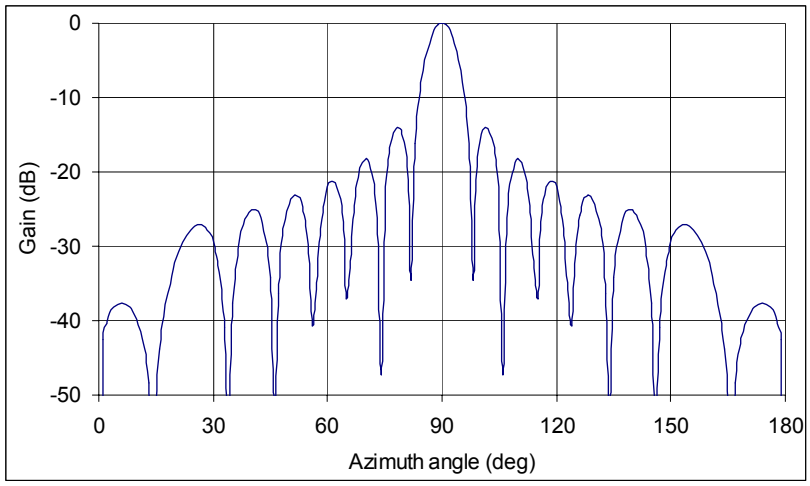

Simulated

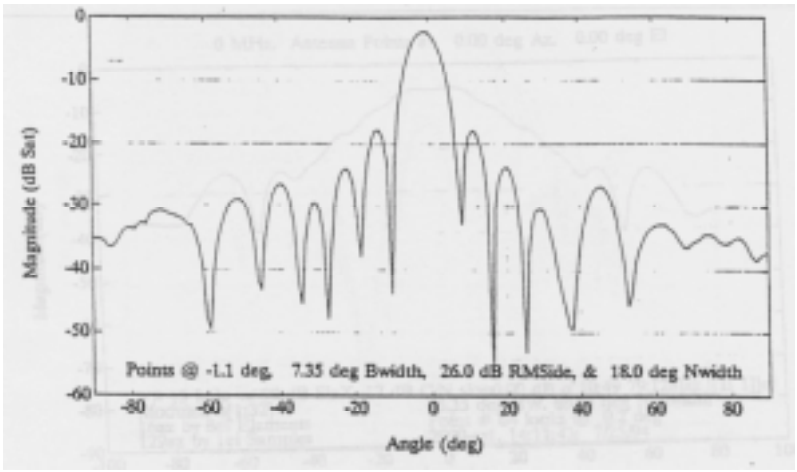

Measured

Figure A2: Simulated and measured transmitter azimuth patterns. Note that the measurement and the simulation define the broadside direction as 0^o and 90^o, respectively.

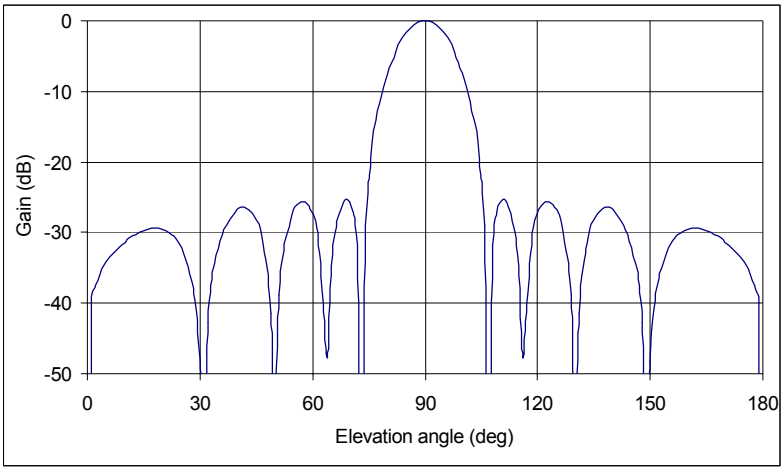

Simulated

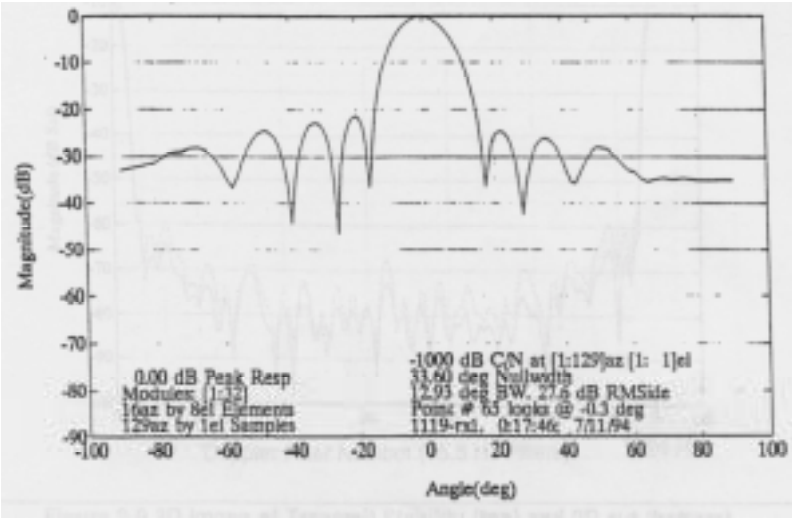

Measured

Figure A3: Simulated and measured transmitter elevation patterns.

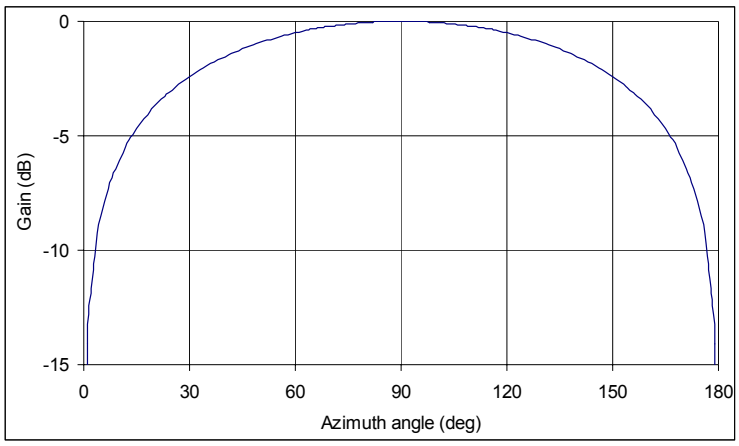

Simulated

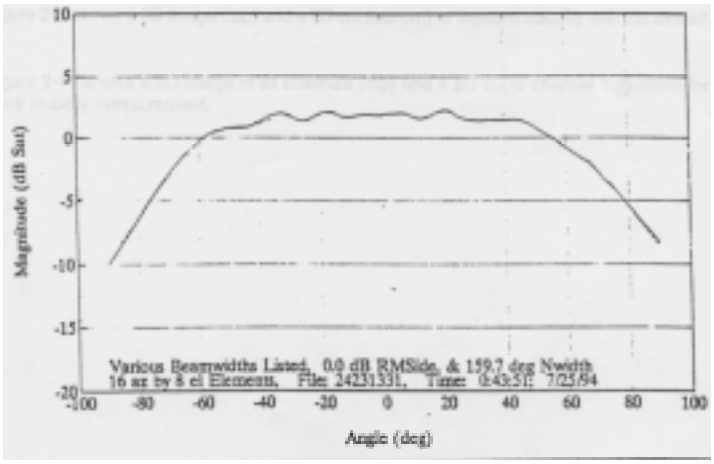

Measured

Figure A4: Simulated and measured receiver azimuth patterns. The steering angle is normally within $\pm 60^0$, so there is no need to modify the simulated pattern to fit the measured pattern beyond the $\pm 60^0$ region.

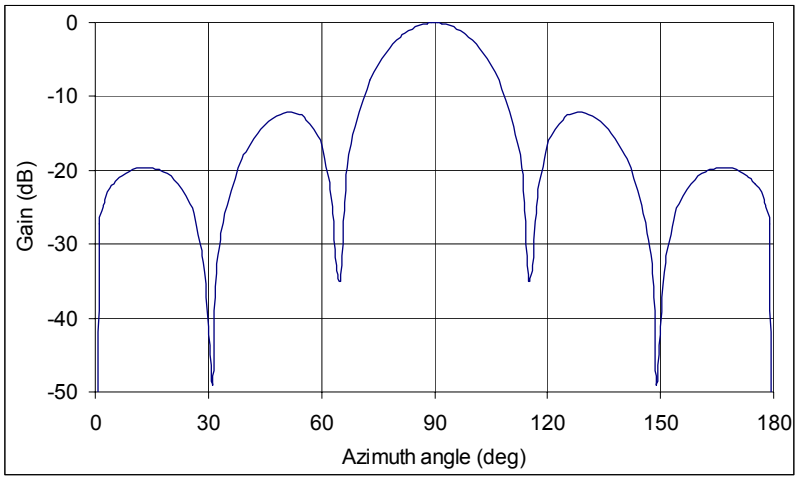

Simulated

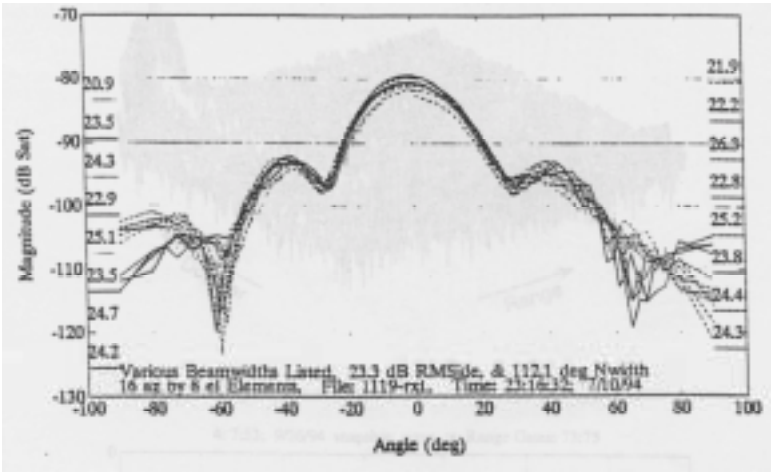

Measured

Figure A5: Simulated and measured receiver elevation patterns.

During Flight 5 only the signals of the central 22 receiving modules were digitally recorded. The flight path of Flight 5 is in the Baltimore-Washington area. The mainlobe area for the data cube #5-575 is mainly flat farmland (range bins 200-400, 500 – 600 for example) and bay water (range bins 400-500, for example). The clutter profile against range in the analogue sum channel is shown in Figure A6. There is a signal leakage in range bin 68, and the useful clutter data are from around range bin 200 to the end.

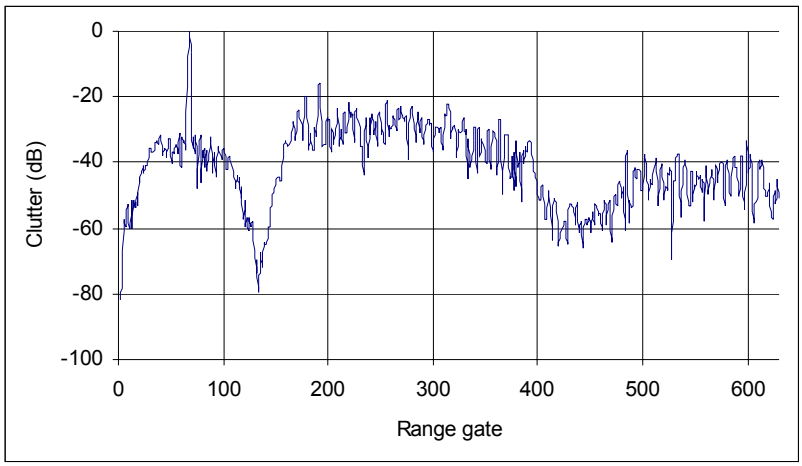

Figure A6: Clutter profile against range.

From the radar equation, clutter power is proportional to $1/R^3$. If the SMI method is used to compute the covariance matrix, the $1/R^3$ range effect on the clutter data is better to be removed. Otherwise, statistics of the close range data play a more important role in the covariance matrix than that of the far range data. The clutter profile against range, after the $1/R^3$ range effect is moved, is shown in Figure A7.

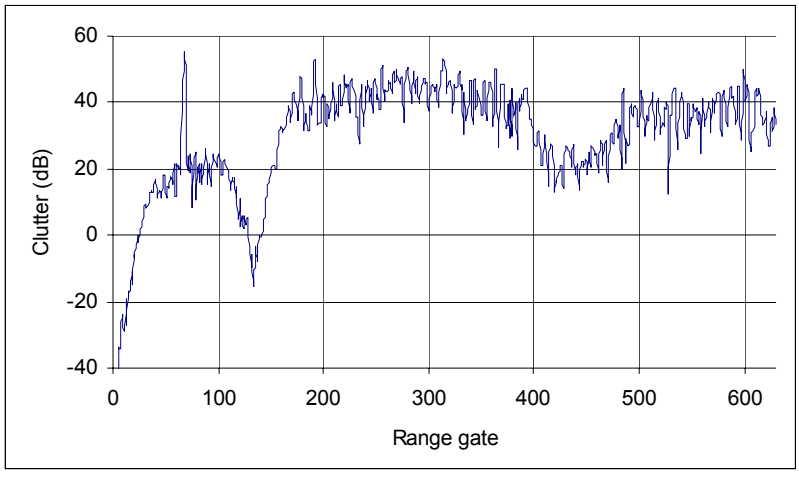

Figure A7: Clutter profile against range after the $1/R^3$ range effect is moved.

The resulting clutter profile is almost levelled after the range effect is removed, though the clutter intensity is still slightly lower at the far range. This is contributed by two factors: the shape of the mainlobe of the transmitter antenna elevation pattern and the clutter profile against grazing angle (Dong, 2004). However, these two factors are not further taken into account when the SMI method is applied to the data to compute the covariance matrix.

Invariance of the Inverse of the Covariance Matrix and the Resultant Pre-built STAP Processor

Yunhan Dong

AUSTRALIA

DEFENCE ORGANISATION	**No. of Copies**
Task Sponsor: DMO, OCAEWCSPO	1
S&T Program	
Chief Defence Scientist FAS Science Policy AS Science Corporate Management Director General Science Policy Development	1 Shared
Counsellor Defence Science, London	Doc Data Sheet
Counsellor Defence Science, Washington	Doc Data Sheet
Scientific Adviser to MRDC, Thailand	Doc Data Sheet
Scientific Adviser Joint	1
Navy Scientific Adviser	Doc Data Sht & Dist List
Scientific Adviser – Army	Doc Data Sht & Dist List
Force Scientific Adviser	1
Scientific Adviser to the DMO M&A	Doc Data Sht & Dist List
Systems Sciences Laboratory	
Chief of EWRD Division	Doc Data Sht & Dist List
EWSTIS	1 PDF
Research Leader Microwave Radar, EWRD	Doc Data Sht & Dist List
Head RST, EWRD: Dr J Whitrow	1
Mr S Capon, RST Group, EWRD	1
Dr P Berrey RMA Group, EWRD	1
Task Manager: Mr G Lawrie	1
Author(s): Dr Y Dong, EWRD	1
Head IRS, ISRD: Dr N Stacy	1
Dr J Fabrizio, ISRD	1
Head RFS, WSD: Dr A Szabo	1
DSTO Library and Archives	
Library Edinburgh	1
Defence Archives	1
Capability Development Group	
Director General Maritime Development	Doc Data Sheet
Director General Capability and Plans	Doc Data Sheet
Assistant Secretary Investment Analysis	Doc Data Sheet
Director Capability Plans and Programming	Doc Data Sheet
Director Trials	Doc Data Sheet

Chief Information Officer Group

Deputy CIO	Doc Data Sheet
Director General Information Policy and Plans	Doc Data Sheet
AS Information Strategy and Futures	Doc Data Sheet
AS Information Architecture and Management	Doc Data Sheet
Director General Australian Defence Simulation Office	Doc Data Sheet
Director General Information Services	Doc Data Sheet

Strategy Group

Director General Military Strategy	Doc Data Sheet
Director General Preparedness	Doc Data Sheet
Assistant Secretary Governance and Counter-Proliferation	Doc Data Sheet

Navy

Maritime Operational Analysis Centre, Building 89/90 Garden Island Sydney NSW	Doc Data Sht & Dist List
Deputy Director (Operations)	
Deputy Director (Analysis)	
Director General Navy Capability, Performance and Plans, Navy Headquarters	Doc Data Sheet
Director General Navy Strategic Policy and Futures, Navy Headquarters	Doc Data Sheet

Air Force

SO (Science) - Headquarters Air Combat Group, RAAF Base, Williamtown NSW 2314	Doc Data Sht & Exec Summ

Army

ABCA National Standardisation Officer Land Warfare Development Sector, Puckapunyal	e-mailed Doc Data Sheet
SO (Science) - Land Headquarters (LHQ), Victoria Barracks NSW	Doc Data Sht & Exec Summ
SO (Science), Deployable Joint Force Headquarters (DJFHQ) (L), Enoggera QLD	Doc Data Sheet

Joint Operations Command

Director General Joint Operations	Doc Data Sheet
Chief of Staff Headquarters Joint Operations Command	Doc Data Sheet
Commandant ADF Warfare Centre	Doc Data Sheet
Director General Strategic Logistics	Doc Data Sheet

Intelligence and Security Group

DGSTA Defence Intelligence Organisation	1
Manager, Information Centre, Defence Intelligence Organisation	1 (PDF)
Assistant Secretary Capability Provisioning	Doc Data Sheet

Assistant Secretary Capability and Systems	Doc Data Sheet
Assistant Secretary Corporate, Defence Imagery and Geospatial Organisation	Doc Data Sheet

Defence Materiel Organisation

Deputy CEO	Doc Data Sheet
Head Aerospace Systems Division	Doc Data Sheet
Head Maritime Systems Division	Doc Data Sheet
Chief Joint Logistics Command	Doc Data Sheet

Defence Libraries

Library Manager, DLS-Canberra	Doc Data Sheet

OTHER ORGANISATIONS

National Library of Australia	1
NASA (Canberra)	1
State Library of South Australia	1

UNIVERSITIES AND COLLEGES

Australian Defence Force Academy

Library	1
Head of Aerospace and Mechanical Engineering	1
Serials Section (M list), Deakin University Library, Geelong, VIC	1
Hargrave Library, Monash University	Doc Data Sheet
Librarian, Flinders University	1

OUTSIDE AUSTRALIA

INTERNATIONAL DEFENCE INFORMATION CENTRES

US Defense Technical Information Center	1 PDF
UK Dstl Knowledge Services	2
Canada Defence Research Directorate R&D Knowledge & Information Management (DRDKIM)	1
NZ Defence Information Centre	1

ABSTRACTING AND INFORMATION ORGANISATIONS

Library, Chemical Abstracts Reference Service	1
Engineering Societies Library, US	1
Materials Information, Cambridge Scientific Abstracts, US	1
Documents Librarian, The Center for Research Libraries, US	1

INFORMATION EXCHANGE AGREEMENT PARTNERS

National Aerospace Laboratory, Japan	1

National Aerospace Laboratory, Netherlands 1

UNITED STATES AIR FORCE

AFRL, Rome, NY: Dr M Davis 1

SPARES 5

Total number of copies: 41 Printed: 38 PDF: 3

DEFENCE SCIENCE AND TECHNOLOGY ORGANISATION
DOCUMENT CONTROL DATA

1. PRIVACY MARKING/CAVEAT (OF DOCUMENT)

2. TITLE

Approximate Invariance of the Inverse of the Covariance Matrix and the Resultant Pre-built STAP Processor

3. SECURITY CLASSIFICATION (FOR UNCLASSIFIED REPORTS THAT ARE LIMITED RELEASE USE (L) NEXT TO DOCUMENT CLASSIFICATION)

Document	(U)
Title	(U)
Abstract	(U)

4. AUTHOR(S)

Yunhan Dong

5. CORPORATE AUTHOR

Systems Sciences Laboratory
PO Box 1500
Edinburgh South Australia 5111 Australia

6a. DSTO NUMBER	6b. AR NUMBER	6c. TYPE OF REPORT	7. DOCUMENT DATE
DSTO-RR-0291	AR-013-364	Research Report	March 2005

8. FILE NUMBER	9. TASK NUMBER	10. TASK SPONSOR	11. NO. OF PAGES	12. NO. OF REFERENCES
2005/1022833	AIR 02/232	DMO OCAEWCSPO	68	27

13. URL on the World Wide Web

http://www.dsto.defence.gov.au/corporate/reports/DSTO-RR- 0291.pdf

14. RELEASE AUTHORITY

Chief, Electronic Warfare and Radar Division

15. SECONDARY RELEASE STATEMENT OF THIS DOCUMENT

Approved for public release

OVERSEAS ENQUIRIES OUTSIDE STATED LIMITATIONS SHOULD BE REFERRED THROUGH DOCUMENT EXCHANGE, PO BOX 1500, EDINBURGH, SA 5111

16. DELIBERATE ANNOUNCEMENT

No Limitations

17. CITATION IN OTHER DOCUMENTS Yes

18. DEFTEST DESCRIPTORS

Adaptive signal processing
Airborne radar
Phased arrays
Covariance

19. ABSTRACT

Space-time adaptive processing (STAP) has been proven to be optimum in scenarios where an airborne phased-array radar is used to search for moving targets. The STAP requires the inverse of the covariance matrix (ICM) of undesired signals. The computation of the real-time ICM is impractical at current computer speeds. Proposing two Theorems, this report indicates that the ICM is approximately invariant if radar and platform parameters remain unchanged. A pre-built STAP (PSTAP) processor is then proposed. Both the simulated data from a generic airborne phased array radar model and real data collected by the multi-channel airborne radar measurement (MCARM) system are processed to verify the processor. Results indicate that the performance of the proposed PSTAP processor is the same as that of the real-time STAP processor.